The Astrophysical Journal, 1008:197 (19pp), 2026 September 10 https://doi.org/10.3847/1538-4357/ae91e6
© 2026. The Author(s). Published by the American Astronomical Society.
OPEN ACCESS

MEOW: The Increase in the Obscured-AGN Fraction in Mid-IR from $0 \leqslant z \leqslant 6$ with JWST MIRI

Teodora-Elena Bulichi[1,2], Gene C. K. Leung[1], Anna-Christina Eilers[1,2], Pablo G. Pérez-González[3], Guillermo Barro[4], Steven L. Finkelstein[5,6], Micaela B. Bagley[5,6], Anton M. Koekemoer[7], Bren E. Backhaus[8], Mark Dickinson[9], Seiji Fujimoto[10,11], Norman A. Grogin[7], Dale D. Kocevski[12], Ray A. Lucas[7], Fabio Pacucci[13], Nor Pirzkal[7], Elia Pizzati[13], Jan-Torge Schindler[14], Alberto Traina[15], and Guang Yang (杨光)[16]
[1] Massachusetts Institute of Technology, Kavli Institute for Astrophysics and Space Research, 77 Massachusetts Avenue, Cambridge, MA 02139, USA; teob1823@mit.edu
[2] Department of Physics, Massachusetts Institute of Technology, 77 Massachusetts Avenue, Cambridge, MA 02139, USA
[3] Centro de Astrobiología (CAB), CSIC-INTA, Ctra. de Ajalvir km 4, Torrejón de Ardoz, E-28850, Madrid, Spain
[4] Department of Physics, University of the Pacific, Stockton, CA 90340, USA
[5] Department of Astronomy, The University of Texas at Austin, Austin, TX, USA
[6] Cosmic Frontier Center, The University of Texas at Austin, Austin, TX, USA
[7] Space Telescope Science Institute, 3700 San Martin Drive, Baltimore, MD 21218, USA
[8] Department of Physics and Astronomy, University of Kansas, Lawrence, KS 66045, USA
[9] NSF's National Optical-Infrared Astronomy Research Laboratory, 950 N. Cherry Avenue, Tucson, AZ 85719, USA
[10] David A. Dunlap Department of Astronomy and Astrophysics, University of Toronto, 50 St. George Street, Toronto, Ontario, M5S 3H4, Canada
[11] Dunlap Institute for Astronomy and Astrophysics, 50 St. George Street, Toronto, Ontario, M5S 3H4, Canada
[12] Department of Physics and Astronomy, Colby College, Waterville, ME 04901, USA
[13] Center for Astrophysics | Harvard & Smithsonian, Cambridge, MA 02138, USA
[14] Hamburger Sternwarte, University of Hamburg, Gojenbergsweg 112, D-21029 Hamburg, Germany
[15] Istituto Nazionale di Astrofisica (INAF)—Osservatorio di Astrofisica e Scienza dello Spazio (OAS), via Gobetti 101, I-40129 Bologna, Italy
[16] Nanjing Institute of Astronomical Optics & Technology, Chinese Academy of Sciences, Nanjing 210042, People's Republic of China
Received 2026 March 23; revised 2026 June 26; accepted 2026 July 17; published 2026 September 3

Abstract

Obscured active galactic nuclei (AGNs) are often invoked to explain the rapid emergence of young quasars at high redshift and are crucial for building a complete census of AGN activity and black hole growth. The advent of the James Webb Space Telescope (JWST) extends the discovery space for obscured AGNs into the mid-IR with unprecedented precision through reprocessed dust emission. In this work, we use deep JWST Mid-Infrared Instrument (MIRI) imaging from the MIRI Early Obscured-AGN Wide Survey (MEOW), together with existing JWST Near Infrared Camera, spectroscopic, and Hubble Space Telescope imaging data, to identify a previously unrecognized population of obscured AGNs out to $z \approx 6$. Using spectral energy distribution modeling of the MIRI-detected sources, we identify 883 AGNs over an area of ~131 arcmin^2 and construct the AGN bolometric luminosity function, including both obscured and unobscured sources, across 5 redshift bins. We find an excess in AGN abundance relative to UV-selected AGN luminosity functions, indicating a substantial obscured population missed by optical/UV surveys, with the inferred obscured fraction increasing with redshift and reaching ~98–99% in our highest-redshift bin, $4.5 < z < 6$. We also find higher AGN abundances and obscured fractions than X-ray-based studies, consistent with a previously unrecognized population of heavily obscured, Compton-thick AGN revealed by mid-IR selection. These results suggest that a large fraction of supermassive black hole growth at early times occurs during heavily obscured phases largely inaccessible at other wavelengths.

Unified Astronomy Thesaurus concepts: Active galactic nuclei (16); Infrared galaxies (790); James Webb Space Telescope (2291)

Materials only available in the online version of record: machine-readable table

1. Introduction

The existence of quasars powered by supermassive black holes (SMBHs) with masses attaining $\sim 10^9\,M_\odot$ within the first billion years of cosmic history (e.g., D. J. Mortlock et al. 2011; C. Mazzucchelli et al. 2017; A.-C. Eilers et al. 2020; X. Fan et al. 2023) presents a significant challenge for theoretical models of black hole growth. In the standard picture, and following the Soltan argument (A. Soltan 1982), SMBHs are thought to assemble their mass through gas accretion, observed during phases of active galactic nucleus (AGN) or quasar activity. Even under the idealized assumption of continuous accretion at the Eddington limit, the time required to grow these objects from stellar remnants is comparable to the age of the Universe at these redshifts, $t_Q \sim 10^8$–10^9 yr, assuming a radiative efficiency corresponding to the cosmic average $\epsilon_{\rm rad} \approx 10\%$ (e.g., M. Volonteri 2010; K. Inayoshi et al. 2020; A.-C. Eilers et al. 2021; F. Pacucci & A. Loeb 2022). Thus, how such massive black holes grew so rapidly, and under which physical conditions this growth occurred, remain key open questions.

The SMBH growth timescale at high redshift can be constrained by measuring the ionizing imprint signatures of quasars on the surrounding intergalactic medium (IGM), since the gas responds to changes in the ionizing output over a finite

Original content from this work may be used under the terms of the Creative Commons Attribution 4.0 licence. Any further distribution of this work must maintain attribution to the author(s) and the title of the work, journal citation and DOI.

timescale. In practice, this has been probed using Lyα proximity zones ($z \approx 6$; A.-C. Eilers et al. 2017), Lyα damping wings at higher redshifts ($z \gtrsim 6$; F. B. Davies et al. 2019), and, more recently, spatially extended ionized nebulae around quasars (D. Ďurovčíková et al. 2025). All of these tracers consistently point toward surprisingly short lifetimes, as low as $t_Q \lesssim 10^4$ yr (A.-C. Eilers et al. 2017, 2018; F. B. Davies et al. 2019; I. T. Andika et al. 2020; A.-C. Eilers et al. 2020; K. A. Morey et al. 2021; S. Satyavolu et al. 2023; D. Ďurovčíková et al. 2024, 2025). Moreover, population-level constraints on UV-bright duty cycles have independently supported these unexpectedly short timescales (J. Arita et al. 2023; A.-C. Eilers et al. 2024; E. Pizzati et al. 2024; J. Huang et al. 2026; J.-T. Schindler et al. 2026; F. Wang et al. 2026). Taken together, these findings underscore the pressing need to reassess our understanding of SMBH growth over cosmic history.

This intriguing tension has motivated two main scenarios that could explain the observations and the early SMBH growth—namely (i) radiatively inefficient "super-Eddington" accretion, allowing for a more rapid mass buildup (e.g., K. Inayoshi et al. 2016; E. Pezzulli et al. 2016; M. C. Begelman & M. Volonteri 2017; J. A. Regan et al. 2019; F. B. Davies et al. 2020; F. Huško et al. 2025; S. Obuchi et al. 2026), possibly even starting from heavier seeds resulting from, e.g., direct collapse (e.g., Z. Haiman et al. 1997; V. Bromm & A. Loeb 2003; M. C. Begelman et al. 2006; M. Volonteri et al. 2008; J. H. Wise et al. 2019; A. Lupi et al. 2021; F. Pacucci et al. 2026), and/or (ii) heavily dust-obscured phases that attenuate the ionizing output and suppress UV-bright signatures of accretion (e.g., P. F. Hopkins et al. 2008; M. Polletta et al. 2008; A. Merloni et al. 2014; F. Vito et al. 2018; J. Lyu et al. 2024). In the latter case, recent duty-cycle estimates imply that $\sim$100 obscured quasars must exist for every unobscured one at $z \gtrsim 6$ in order to reconcile the observed SMBH masses with the observed growth timescales (A.-C. Eilers et al. 2024; J. Huang et al. 2026; J.-T. Schindler et al. 2026), far exceeding the obscured fractions of $\sim$20–50% inferred in the local Universe, which rely predominantly on hard X-ray observations (D. Burlon et al. 2011; K. Iwasawa et al. 2012; Y. Ueda et al. 2014; J. Buchner et al. 2015; T. Liu et al. 2017; L. Zappacosta et al. 2018; K. Iwasawa et al. 2020).

While theoretical predictions (M. Trebitsch et al. 2019; Y. Ni et al. 2020; F. Vito et al. 2022; J. S. Bennett et al. 2024), indirect measurements from the interstellar medium (ISM) constraints (R. Gilli et al. 2022), and decades of multi-wavelength searches for obscured AGNs (see reviews by R. C. Hickox & D. M. Alexander 2018; A. Sajina et al. 2022) point toward a redshift evolution of the obscured fraction (see also A. Peca et al. 2025), constraining its value at high redshift (i.e., $z \gtrsim 3$) has remained challenging: Strong gas and dust columns, coupled with cosmological dimming, render X-ray surveys that are increasingly incomplete at early times, with detection efficiencies dropping to $\lesssim$30–40% for obscured AGNs (F. Vito et al. 2018), while also making redshift constraints more challenging due to their faint or absent optical/UV counterparts. Moreover, recent radio studies suggest that the population of Compton-thick AGNs at early epochs ($z \approx 3$) may be substantially underestimated in cosmic X-ray background models, pointing to a heavily obscured-AGN population that is larger by a factor of $\sim$2–3 than currently accounted for (G. Mazzolari et al. 2026).

An alternative tracer of obscured accretion emerges in the rest-frame near-IR, redshifted to mid-IR at high redshift, where the hot circumnuclear dust reradiates the absorbed AGN emission (e.g., M. Lacy et al. 2004; D. Stern et al. 2005; A. Alonso-Herrero et al. 2006; J. L. Donley et al. 2012; R. J. Assef et al. 2013; C.-T. Ling et al. 2026). However, before the James Webb Space Telescope (JWST), mid-IR studies at $z \gtrsim 2$ were severely limited by the restricted wavelength coverage and sensitivity of previous facilities, particularly beyond $\sim$8 μm. This limitation has been overcome by JWST's Mid-Infrared Instrument (MIRI; G. S. Wright et al. 2023), which offers nine broadband filters in the wavelength range 5–26 μm, covering the hot-dust spectral features of AGNs out to $z \approx 8$. Relative to its predecessor, Spitzer, MIRI achieves $\sim$10–100$\times$ higher sensitivity and $\sim$8$\times$ finer angular resolution at comparable wavelengths, enabling the detection and characterization of obscured SMBH growth with unprecedented precision (e.g., G. Yang et al. 2023; J. Lyu et al. 2024; C.-A. Hsieh et al. 2025).

Moreover, pre-JWST discoveries of individual high-redshift obscured or reddened AGN candidates have further highlighted the importance of this population. For example, S. Fujimoto et al. (2022) identified GNz7q, a compact dust-enshrouded source at $z \simeq 7.19$ that may represent a transition phase between dusty starbursts and unobscured quasars, while R. Endsley et al. (2023) confirmed COS-87259, a heavily obscured, hyperluminous AGN candidate at $z \simeq 6.83$. These findings suggest that obscured accretion may already be common in the reionization era, but a homogeneous statistical census remains necessary to quantify its prevalence, now possible with JWST.

In this paper, we present a homogeneous measurement of the obscured-AGN fraction out to $z \approx 6$ using the MIRI Early Obscured-AGN Wide Survey (MEOW #5407, PI: G. C. K. Leung, R. Endsley, S. L. Finkelstein; G. C. K. Leung et al. 2026). This program adds deep MIRI 10 and 21 μm imaging over $\sim$95 arcmin^2 in the Great Observatories Origins Deep Survey (GOODS; M. Giavalisco et al. 2004) fields. We supplement our analysis with data from SMILES, which cover $\approx$34 arcmin^2 in GOODS-S (G. H. Rieke et al. 2024), with a total area of $\approx$65 arcmin^2 split equally between GOODS-N and GOODS-S. Leveraging MIRI's sensitivity to hot-dust emission, in combination with extensive JWST Near Infrared Camera (NIRCam) imaging, and NIRSpec spectroscopy from JADES (D. J. Eisenstein et al. 2026), NIRCam WFSS from FRESCO (P. A. Oesch et al. 2023), as well as archival coverage from the Hubble Space Telescope (HST), we robustly identify a previously unrecognized population of obscured AGNs at early cosmic times. These observations provide new constraints on SMBH growth pathways that could alleviate the short quasar lifetime tension (e.g., A.-C. Eilers et al. 2018, 2020; D. Ďurovčíková et al. 2025; J.-T. Schindler et al. 2026).

The overall framework of the analysis presented in this paper is illustrated in Figure 1. The text is organized as follows: Section 2 discusses the data acquisition and processing. Section 3 describes the AGN identification through spectral energy distribution (SED) fitting, used simultaneously for redshift determinations and completeness corrections. Section 4 presents the methodology for the luminosity-function measurements, which we use in Section 5 to compute the obscured-AGN fraction. In Section 6, we place our results

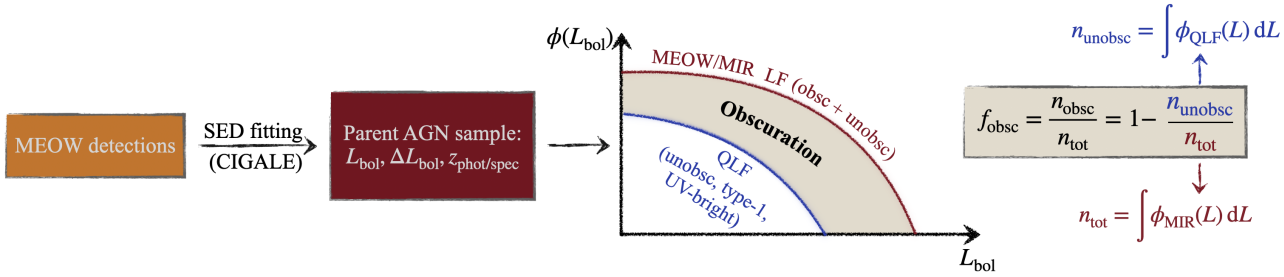


Figure 1. Framework for quantifying the AGN obscured fraction. We illustrate the layout in characterizing obscuration, from the MEOW source detections (Section 2.3), followed by the identification of AGNs, and corresponding bolometric luminosities and uncertainties L_{bol}, ΔL_{bol} (Section 3.3), as well as photometric-redshift determinations (Section 2.5) through SED fitting. These measurements enable the construction of AGN luminosity functions across five redshift bins, incorporating both obscured and unobscured populations (Section 4). Finally, we quantify the obscured fraction as a function of luminosity and redshift by evaluating the excess of MEOW AGNs relative to type-1, unobscured quasars (Section 5.2).

in the context of previous work and discuss the implications for early SMBH growth. Finally, Section 7 summarizes our main findings.

Throughout the paper, we adopt the flat ΛCDM Planck Collaboration et al. (2016) cosmology: $H_0 = 67.66\,\mathrm{km\,s^{-1}\,Mpc^{-1}}$, $\Omega_M = 0.3097$, and $\Omega_\Lambda = 0.6889$.

2. Data

In this section, we describe the data products used for the AGN sample identification (Section 3). A detailed description of the JWST MEOW program, data reduction, source detection, and photometry will be available in G. C. K. Leung et al. (2026), and here we provide a summary of the key procedures.

2.1. MIRI Observations

In this study, we make use of deep MIRI imaging, in F1000W, and F2100W, within the GOODS-N and GOODS-S fields, through the MEOW JWST program. MEOW is designed to uncover the population of heavily obscured SMBHs that remain elusive at optical/UV wavelengths. By coupling these new MIRI observations with existing NIRCam slitless spectroscopy, deep multiwavelength imaging in the GOODS fields, and archival HST data, the survey identifies AGNs through their characteristic hot-dust emission, a well-established tracer of obscured accretion at early cosmic times (see Section 3).

MEOW comprises 74 hr of MIRI imaging over an area of 95 arcmin^2, using the F1000W and F2100W filters. Each pointing includes exposure times of approximately 720 s in F1000W and 3000 s in F2100W, employing the FASTR1 readout and a four-point dither pattern.

Data in GOODS-S are supplemented by F1000W and F2100W observations from SMILES (JWST #1207, PI: G. H. Rieke; G. H. Rieke et al. 2024). SMILES comprises 15 separate pointings over a total area of ∼34 arcmin^2 in GOODS-S, and similarly uses the FASTR1 readout together with a four-point dither pattern. The total exposure time of ∼2.2 hr is divided among eight MIRI filters (F560W, F770W, F1000W, F1280W, F1500W, F1800W, F2100W, and F2550W). For consistency with MEOW, we only make use of the F1000W and F2100W imaging, with integration times of 642 and 2184 s, respectively. Additionally, we employ the same source-detection methodology as in MEOW on the two SMILES F1000W and F2100W images (see Section 2.3).

We additionally incorporate MIRI imaging data in the GOODS fields publicly available as of 2025 September. These include F1000W observations from PIDs 2926 and 4762 in GOODS-N, and PIDs 1283, 4498, and 6511 in GOODS-S. These observations fall completely within the MEOW or SMILES footprints. Lastly, the total survey areas in GOODS-N and GOODS-S are approximately equal, ∼65 arcmin^2.

2.2. MIRI Data Reduction

The data reduction was carried out with the JWST Rainbow pipeline, following the techniques described in Appendix A of P. G. Pérez-González et al. (2024a). More specific details about the MEOW and the supplemental SMILES dataset are given in G. C. K. Leung et al. (2026). In short, the data reduction is based on the official JWST pipeline (v1.19.41, jwst_1413.pmap), with custom modifications in the background subtraction. Specifically, we introduce additional steps, in the "superbackground" subtraction described in the following paragraph, to improve the treatment of spatially varying and small-scale background structures, particularly at the shortest MIRI wavelengths.

We first processed the data through the standard JWST pipeline to obtain an initial mosaic, which we used to detect sources with SExtractor (E. Bertin & S. Arnouts 1996) and generate a segmentation map. From this, we built source masks that flag all detected objects and their extended emission. These source masks were then mapped back to the native pixel grid of each individual calibrated frame, ensuring that only background regions remained unmasked. With astrophysical sources removed, we modeled and subtracted large-scale background structure and then constructed a superbackground image by median-combining the masked, background-normalized exposures. This superbackground was scaled and subtracted from each frame, significantly improving background flatness and suppressing low-frequency instrumental patterns (see also G. Yang et al. 2023; S. Alberts et al. 2024; P. G. Pérez-González et al. 2024b; B. E. Backhaus et al. 2025; G. Östlin et al. 2025). After the data reduction, the resulting 1σ depths are 0.0998 μJy in F1000W and 0.718 μJy in F2100W.

2.3. MIRI Photometry

We detected the MIRI sources using SExtractor version 2.28.2 individually on each of the two filters (F1000W and F2100W), and constructed the MIRI parent sample by requiring sources to be detected in both MIRI filters, with

positional matches within 0.″5 (see Sections 2.4, 3.1). We employed a hot–cold detection scheme, following the framework described in A. Galametz et al. (2013), adopting DEBLEND_MINCONT values of 0.001 and 0.02 for the hot detection scheme, for F1000W and F2100W, respectively, and 0.2 for the cold detection scheme. The cold configuration was optimized for bright, extended sources using conservative detection thresholds, minimum-area requirements, and deblending parameters, while the hot configuration employed more aggressive settings to recover faint sources. The final catalog was constructed by retaining all sources from the cold detection and including hot-detected sources only if their positions lay outside a dilated cold segmentation map. Spurious detections significantly narrower than the point-spread function were removed based on the fraction of flux enclosed within a small aperture.

The MIRI photometry, for both MEOW and the supplemental SMILES F1000W and F2100W images, was measured in circular apertures with radii of 0.″3 in F1000W and 0.″5 in F2100W, and aperture corrections were applied using the MIRI instrument team's flux-calibration products (K. D. Gordon et al. 2025), based on the reference file jwst_miri_apcorr_0014.fits. The photometric uncertainties were estimated by placing the aperture of the same size in nonoverlapping empty/sky regions of the mosaic. Specifically, we computed the median absolute deviation of all fluxes and converted it to an equivalent Gaussian uncertainty by multiplying by 1.48. We then applied the same aperture correction as for the fluxes. Lastly, to account for different depths in different parts of the mosaic, we multiplied the error of each source by the ratio between the value of the error map at the source location and the median value of the error map.

2.4. NIRCam and HST Photometry

The NIRCam and HST photometry are based on the UNICORN project catalogs (v0.89 for GOODS-S, v0.9 for GOODS-N; S. L. Finkelstein et al. 2026, in preparation), which includes all HST/Advanced Camera for Surveys (ACS) and NIRCam data in the MEOW footprints. This is inclusive of the FRESCO survey data in the F182M, F210M, and F444W filters, along with HST data in ACS WFC F435W, F606W, F775W, F814W, and F850L, and WFC3/IR F105W, F125W, F140W, and F160W from the GOODS and CANDELS surveys, all of which cover the full MEOW footprint. Imaging from JADES is available in parts of the MEOW footprint, covering F090W, F115W, F150W, F200W, F210M, F277W, F335M, F356W, F410M, and additionally F210M and F480M in GOODS-S.

The UNICORN catalog uses SExtractor and the hot–cold detection scheme, on a combined F277W+F356W used as the primary detection image, supplemented by F444W as the secondary detection image, as parts of the MEOW footprint are not covered by F277W+F356W. The NIRCam detections were matched with the MIRI sources (Section 2.3), requiring a detection in each F444W, F1000W, and F2100W for our final parent sample (see also Section 3.1). The photometric procedures follow the methodology presented in S. L. Finkelstein et al. (2024), with updates presented in A. J. Taylor et al. (2025), and we refer the reader to these papers for more details.

For each source, we have at least a total of 11 filters to constrain the SED, and the HST coverage aids in identifying the Lyman break and thus helps constrain the redshift for high-z objects more accurately (see Section 2.5).

2.5. Redshift Determination

While for most sources (67% of the AGN sample; see Section 3.3) we have to rely on photometric redshifts, we use the spectroscopic redshift wherever available from CANDELS (N. A. Grogin et al. 2011; A. M. Koekemoer et al. 2011; D. Kodra et al. 2023), JADES (D. J. Eisenstein et al. 2026), and FRESCO (P. A. Oesch et al. 2023). All three programs provide coverage in both GOODS-S and GOODS-N, across multiple redshifts ($z \gtrsim 4.5$ for FRESCO, extended to lower redshifts in CANDELS and JADES). We identify counterparts to our sample by requiring an angular separation smaller than 0.″2. For all the other sources, we obtain two photometric redshifts for each source, one using the code eazy on the NIRCam and HST photometry (Section 2.4), part of the UNICORN catalogs, which fits linear combinations of galaxy templates to the observed photometry to minimize χ^2 across a redshift grid (G. B. Brammer et al. 2008), and the second directly from CIGALE as part of the SED fitting (Section 3.2). We emphasize, however, that the main analysis presented in this paper relies exclusively on the CIGALE photometric redshifts, when spectroscopic redshifts are not available. This choice is motivated by the fact that CIGALE is better suited to the goals of this study, as it models the AGN contribution self-consistently, whereas eazy does not include AGN templates. The eazy counterparts are presented only to provide a comparison between two independent photometric-redshift estimates, and we further explore the impact of this choice on our results in Appendix B.

We show the results from these two methods in Figure 2, highlighting only the sources with $f_{\rm AGN} > 0.1$ (see Section 3.3) and AGN bolometric luminosity $L_{\rm bol} > 10^{44}\,{\rm erg\,s^{-1}}$, used subsequently in our analysis (Sections 4 and 5). In Figure 2, where available, we show the spectroscopic redshift in lieu of eazy and also show for comparison the corresponding CIGALE redshift determinations. We note that for all the analysis of this paper, we reran the SED fitting with the spectroscopic redshifts fixed, where available, and we only show the corresponding CIGALE photo-z in Figure 2 to illustrate the accuracy of redshift determinations as part of the SED fitting.

First, we report an overall good agreement between the photometric-redshift estimates from CIGALE and the corresponding spectroscopic values, with ∼88% of the sources within $|\Delta z| < 1$ (i.e., the size of the luminosity-function redshift bins; Section 4) and a median of $|\Delta z|_{\rm med} \approx 0.17$ from the spectroscopic counterpart. We find that if CIGALE misidentifies the redshift, it tends to generally underestimate it, and we identify seven clear outliers where the code yields photometric redshifts of $z_{\rm CIGALE} \lesssim 1$ for sources with spectroscopic redshifts $z_{\rm spec} \gtrsim 3$. Upon closer inspection, three of these seven sources exhibit large uncertainties in the HST photometry blueward of the Balmer break. The remaining four show degeneracy between low- and high-redshift solutions, with CIGALE preferentially assigning higher weight to the low-redshift fit. The same is true for the four sources with $z_{\rm CIGALE} \approx 1.5$ and $z_{\rm spec} \approx 2.2$. Despite these discrepancies, we find that their impact on our luminosity-function measurements is negligible. Incorporating photometric-redshift uncertainties directly into the luminosity-function computations, by

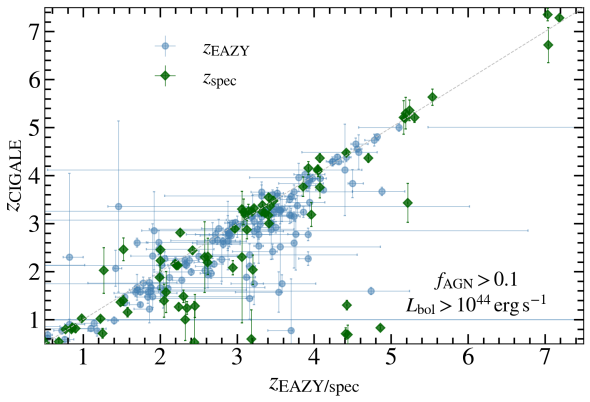


Figure 2. CIGALE redshift estimates compared to eazy (blue) and spectroscopic measurements (green). We show only the sources included in the analysis presented in this paper (Section 4), namely those with $f_{AGN} > 0.1$ and $L_{bol} > 10^{44}$ erg s^{-1}. Overall, the CIGALE redshifts are in good agreement with both the eazy and spectroscopic measurements; however, we identify 41 outliers, as well as a bias toward lower-redshift estimates from CIGALE (see text). Of the 254 sources, 83 have secure spectroscopic redshifts, which are adopted for the analysis in this paper. For the remaining 171, we rely on the CIGALE redshift estimates, noting that the choice between CIGALE and eazy does not affect the population-level results of this work (Appendix B).

perturbing each redshift according to its corresponding uncertainty, leaves the resulting luminosity functions essentially unchanged (Section 4.1). The small number of clear outliers therefore has no significant effect at the population level. Furthermore, adopting spectroscopic redshifts when available helps minimize the uncertainties propagated into the subsequent analyses.

A comparison of the photometric redshifts from CIGALE and eazy shows overall good agreement, though we identify 30 clear outliers out of 171 sources. In six cases, the eazy redshift probability distribution exhibits a secondary peak consistent with the CIGALE solution. An additional 11 eazy estimates are poorly constrained, with uncertainties spanning $\Delta z_{eazy} \gtrsim 3$. For the remaining 13 sources, the CIGALE fits are well constrained, suggesting that the discrepancy likely arises from template degeneracies in eazy, although more systematic effects may also contribute, including the tendency for CIGALE to favor lower-redshift solutions.

As mentioned before, we adopt the CIGALE redshifts for sources without spectroscopic measurements. This choice is motivated by the code's ability to derive redshifts consistently with the full SED fitting, accounting self-consistently for the AGN and galaxy host spectral features, as well as dust reprocessing in IR. We emphasize, however, that our results are not sensitive to the choice between eazy and CIGALE, as the redshift discrepancy for most sources is less than the width of the redshift bins used subsequently in the luminosity-function calculations (Section 4), and the small number of outliers has no statistically significant effect on the overall population. A detailed comparison is presented in Appendix B.

3. AGN Sample

In this section, we discuss the steps undertaken to obtain the complete MIRI AGN sample, which represents the basis of the subsequent analysis of this paper (Sections 4 and 5). We first describe the parent sample on which we performed SED fitting using CIGALE (M. Boquien et al. 2019; G. Yang et al. 2020), then outline the AGN selection criteria, and conclude by assessing the AGN sample completeness.

3.1. Parent Sample

We use the MIRI detections (Section 2.3) to identify and characterize the parent AGN sample (Section 3), with the aim of constructing the redshift and luminosity evolution of the AGN obscured fraction, as depicted in Figure 1.

First, in order to obtain sufficient photometric coverage for SED fitting (see Section 3.2), we match the MIRI detections with the corresponding NIRCam detections (see also Section 2.4), requiring a matching radius/separation of less than $0\farcs5$. For the final parent catalog, we require sources to be detected in each of the three filters: F444W, F1000W, and F2100W. We note that this selection would remove any potential NIRCam dark sources, but upon closer inspection, we did not find any NIRCam dark objects in our sample. We identify a total of 1518 sources in GOODS-N, and 1191 sources in GOODS-S. We note that the difference between the two fields is consistent with the results reported in B. E. Backhaus et al. (2025), where they find a lower source count in SMILES (GOODS-S), compared to MEGA/CEERS (Extended Groth Strip, or EGS). Nonetheless, the overall distribution of sources in type (see Section 3.3) and redshift bins is consistent between the two fields (see Figure 4), with the exception of $z \approx 5$, where GOODS-N is overdense (E. Daddi et al. 2009; C. M. Casey 2016; T. B. Miller et al. 2018; X. Lin et al. 2026). Lastly, we find that the field-to-field variations do not impact our luminosity functions (Section 4; see also E. P. Vidal et al. 2026) and/or obscured fractions (Section 5.2), including in the highest-redshift bin where small number statistics lead to larger uncertainties.

3.2. SED Fitting

In order to identify the AGNs, as well as their key properties (e.g., luminosity, obscured fraction), we perform SED modeling on all sources using CIGALE v2022.1 (M. Boquien et al. 2019; G. Yang et al. 2020, 2022), and on the MIRI and existing NIRCam/HST filters (see Section 2.3). We show all the customized CIGALE parameters in Table 1, following a similar approach to G. Yang et al. (2023), and provide a short description of each component in the following discussion. All the other parameters not listed in the table adopt the default values of CIGALE. In total, CIGALE fits 13 free parameters, with an input of at least 11 and a maximum of 20 photometric points, depending on the overlap with existing NIRCam/HST data (see Section 2.4).

For the stellar-population modeling, we employ a standard delayed star formation history, with the *e*-folding time allowed to vary between 0.5 and 5 Gyr and the stellar age allowed to vary between 0.1 and 5 Gyr. We adopt a G. Chabrier (2003) initial mass function (IMF), and a constant metallicity $Z = 0.02$. We additionally include a nebular emission module (J. A. Villa-Vélez et al. 2021) that assumes the same gas metallicity as the stellar metallicity, $Z = 0.02$, and a constant ionization parameter $\log U = -2$ for the H II regions.

The effects of galactic dust are modeled assuming a D. Calzetti et al. (2000) dust attenuation law, extended into the far-UV (i.e., at wavelengths shorter than the nominal Calzetti range, down to the Lyman break), following the prescriptions of C. Leitherer et al. (2002), as well as

Table 1
CIGALE Model Parameters

Module	Parameter	Symbol	Values
Star formation history `sfhdelayed`	Stellar e-folding time	$\tau_{\rm star}$	0.5, 1, 2, 3, 4, 5 Gyr
	Stellar age	$t_{\rm star}$	0.1, 0.2, 0.5, 1, 2, 3, 4, 5 Gyr
Simple stellar population `bc03`	Initial mass function	⋯	G. Chabrier (2003)
	Metallicity	Z	0.02
Nebular emission `nebular`	Ionization parameter	$\log U$	−2.0
	Gas metallicity	$Z_{\rm gas}$	0.02
Dust attenuation `dustatt_modified_starburst`	Color excess of nebular lines	$E(B-V)_{\rm line}$	0, 0.02, 0.05, 0.1, 0.2, 0.3, 0.4, 0.5, 0.7, 0.9, 1.0
	Ratio between line and continuum $E(B-V)$	$\frac{E(B-V)_{\rm line}}{E(B-V)_{\rm cont}}$	1
Galactic dust emission `dl2014`	PAH mass fraction	$q_{\rm PAH}$	0.47, 2.5, 7.32
	Minimum radiation field	$U_{\rm min}$	0.1, 1.0, 10, 50
	Fraction of PDR emission	γ	0.01, 0.02, 0.05, 0.1, 0.2, 0.5, 0.9
AGN (UV-to-IR) emission `skirtor2016`	Average edge-on optical depth at 9.7 μm	$\tau_{9.7}$	3, 5, 7, 9, 11
	Viewing angle	$\theta_{\rm AGN}$	70° (type-2)
	AGN contribution to the 3–30 μm luminosity	$f_{\rm AGN}$	0, 0.05, 0.1–0.9 (step 0.1), 0.99
	Wavelength range where $f_{\rm AGN}$ is defined	$\lambda_{\rm AGN}$	3–30 μm
	$E(B-V)$ for the extinction in the polar direction	*EBV*	0, 0.05, 0.1, 0.15, 0.2, 0.3
Redshift+IGM `redshifting`	Source redshift	z	0–8.0 (step 0.1)

Note. For parameters not listed here, default values are being adopted.

considering galactic dust emission according to the model described in B. T. Draine et al. (2014). The latter is assumed to equal the attenuated luminosity of starlight, and is split between diffuse emission and emission from photodissociation regions (PDRs), corresponding to star formation sites. In both regions, the mass fraction of polycyclic aromatic hydrocarbon (PAH) is set by the same parameter $q_{\rm PAH}$, which we allow to vary between three values: 0.47, 2.5, and 7.32. The radiation fields of the two dust emission regions are controlled by the minimum radiation parameter ($U_{\rm min}$) and the γ parameter (see Table 1). Namely, the dust radiation from the diffuse region is set by $U_{\rm min}$, while the PDR's dust emission ranges from $U_{\rm min}$ to a fixed maximum value $U_{\rm max} = 10^7$, and the relative contribution of the two components is controlled by the parameter γ.

The AGN emission, covering the UV-to-IR wavelength range, is described via CIGALE's `skirtor2016` module, assuming a clumpy torus model described in M. Stalevski et al. (2012, 2016). We allow the optical depth at 9.7 μm to vary between all available values: 3, 5, 7, 9, and 11. For all the fits, we assume that the AGNs are type-2, set by the viewing angle (see Table 1). We emphasize, however, that this choice is independent of how obscuration is quantified later (Section 5.2; see also Figure 1). Its only impact is on the bolometric luminosity estimate, through the different AGN contribution at bluer wavelengths in type-1 and type-2 templates, but the differences are mild as the luminosity is strongly constrained by the rest-frame near-IR signature. As explained in previous studies (Q. Ni et al. 2021; G. Yang et al. 2021; F. Zou et al. 2022; G. Yang et al. 2023), including type-1 models would cause a strong degeneracy between AGN and stellar contributions in the UV-optical regime, making it more difficult to identify the obscured AGNs, which are the focus of this work. We also expect the number of type-1 AGNs to be rarer, especially at high redshift (e.g., M. Lacy et al. 2015). We note, however, that this choice does not affect our population results, such as luminosity functions (see Appendix B).

The relative AGN contribution to the 3–30 μm luminosity is set by $f_{\rm AGN}$, which covers the AGN dust emission, similar to the methodology of G. Yang et al. (2023). We emphasize that our customized wavelength range differs from the default CIGALE definition of $f_{\rm AGN}$, which is computed over 8–1000 μm, and that alternative definitions have also been adopted in the literature. For example, A. Kirkpatrick et al. (2015) compute an analogous $f_{\rm AGN}$ over 5–15 μm. Despite these differences in wavelength coverage, we find good agreement for the sources used in our luminosity functions that overlap with A. Kirkpatrick et al. (2015). Of the 10 overlapping AGNs, 9 are assigned the same classification, either mixed or AGN-dominated, in both studies. The only exception has $f_{\rm AGN} \approx 0.3$ in our sample, corresponding to a mixed classification, but $f_{\rm AGN} = 0.07$ in A. Kirkpatrick et al. (2015), corresponding to a star-forming (SF) classification. We note that this source is faint, with an inferred luminosity of order $\sim 10^{44}$ erg s^{-1} in both studies, and therefore its inferred AGN contribution may be particularly sensitive to the wavelength coverage and sensitivity of the observations. Similar to G. Yang et al. (2023), we model both the dust on the torus scale, as well as the polar dust extinction via the *EBV* parameter.

Lastly, we allow CIGALE to fit the redshift of all sources (see Section 2.5), using a linear grid $z = 0-8$, in steps of $\Delta z = 0.1$. For the sources with spectroscopic redshift, we fix those values for all the SED fitting.

We show four examples of SED fitting in Figure 3, along with the image cutouts in the two MEOW filters, F1000W and F2100W, as well as the corresponding F444W NIRCam image for each source. The reference sources were chosen at four

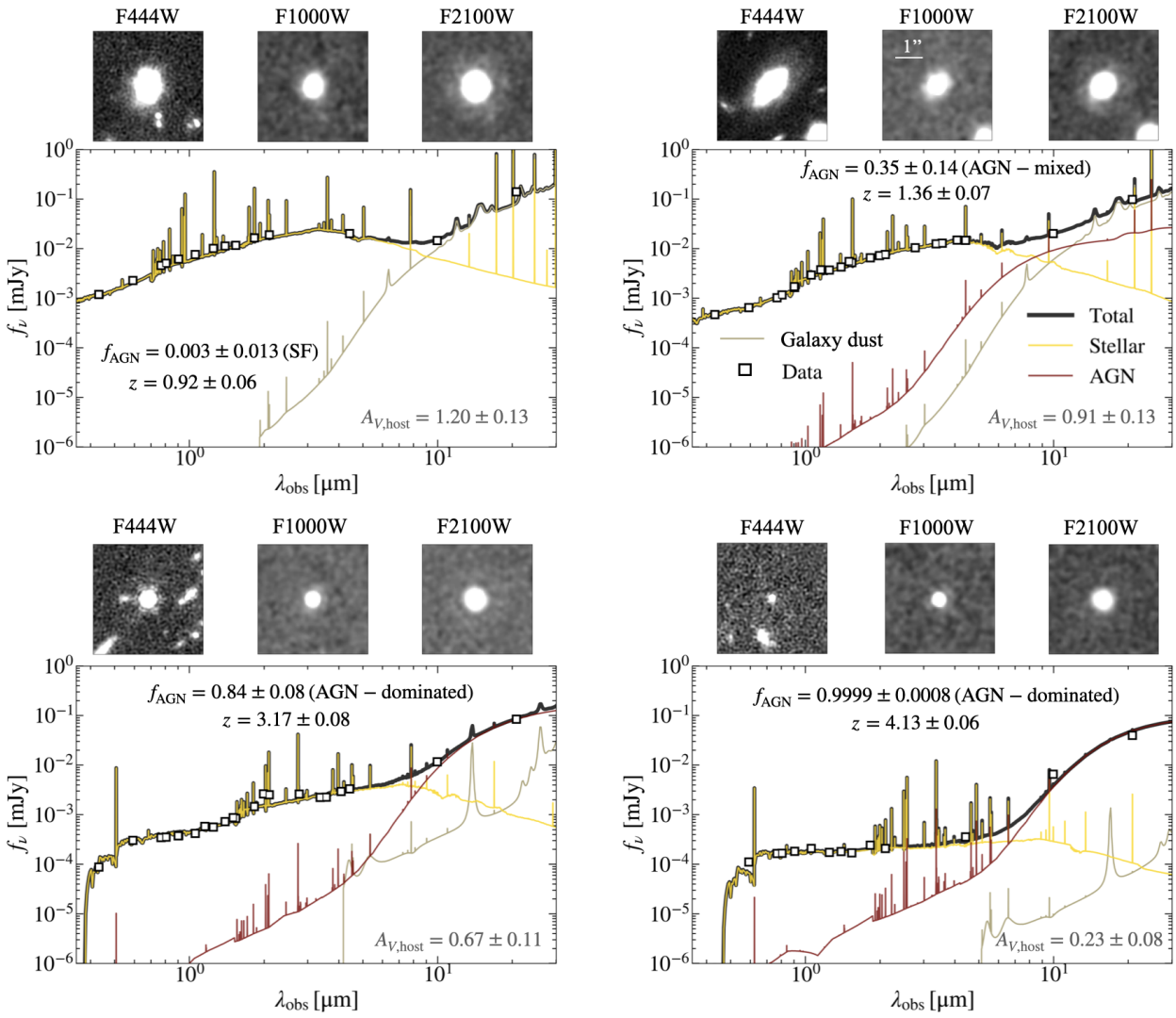


Figure 3. Examples of SED fits, and corresponding cutouts in the F444W, F1000W, and F2100W filters, for an SF object at $z = 0.92$ (top-left), and three AGNs, with increasing $f_{\rm AGN}$ (quoted on the plot) at $z = 1.36$ (top-right), $z = 3.17$ (bottom-left), and $z = 4.13$ (bottom-right). Photometric measurements are plotted as open black squares; uncertainties are included but not visible due to the high signal-to-noise. In the first two cases, the negligible AGN contribution in the SF system and the modest enhancement above the dust component in the top-right object support their classifications. The last two objects are clearly AGN-dominated, highlighted by the mid-IR bump that can only be explained through the hot AGN circumnuclear dust, which exceeds the galactic dust responsible for attenuating the blue stellar continuum.

different redshifts $z = 0.92$, $z = 1.36$, $z = 3.17$, and $z = 4.13$, as well as with different AGN contributions, quantified by $f_{\rm AGN}$. In all cases, we highlight the individual contributions of the stellar component, the AGN, and the galaxy dust to the total SED. While both the galaxy dust and AGN components emit in the mid-IR, which can lead to degeneracies in the fitting and potentially affect the AGN identification, the use of energy balance in CIGALE provides an additional constraint. In particular, the galaxy dust emission is tied to the attenuation of the blue stellar continuum (which we quantify via $A_{V,\rm host}$, shown in Figure 3), helping to distinguish it from AGN-heated dust. This is especially evident in the bottom-right panel of Figure 3, where the mid-IR bump can only be explained by the AGN dust component: The stellar continuum shows little attenuation at bluer wavelengths ($A_{V,\rm host} = 0.23 \pm 0.08$), indicating very low levels of host dust. Therefore, we expect any mid-IR degeneracy to have only a minor impact at the population level, affecting mostly the sources with subdominant AGN contributions (i.e., $f_{\rm AGN} \lesssim 0.5$). Additionally, we verified that including sub-mm constraints for the high-redshift sources does not affect the SED fits or the resulting $f_{\rm AGN}$ classifications. This suggests that our AGN identifications are not driven by confusion with heavily obscured SF systems. This point is discussed further in G. C. K. Leung et al. (2026).

Lastly, we note that the four sources presented in the $5'' \times 5''$ cutouts above the SED fits exhibit diverse morphologies in the NIRCam imaging, while the corresponding MIRI emission appears more compact for the sources with higher inferred AGN contributions. However, given the small number of examples shown here, these cutouts are not sufficient to draw firm conclusions about the broader source population, and we defer a detailed population-level analysis of AGN morphology to future work.

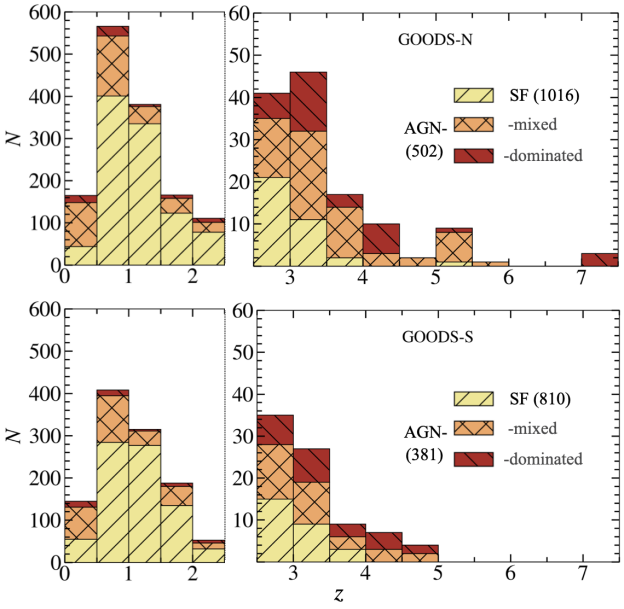


Figure 4. Stacked histogram of the redshift distribution for sources in GOODS-N (top) and GOODS-S (bottom). SF systems dominate both fields, except at $z \gtrsim 4$, where the MIRI selection becomes increasingly sensitive to AGN and mixed sources. Despite the difference in overall number counts (see text), the relative fractions of SF, composite, and AGN sources remain broadly consistent across the two fields.

Based on the CIGALE SED-fitting results, we further identify and characterize the parent AGN sample in the following subsection. We additionally visually inspected all sources and removed spurious objects ($\sim$1% of the total objects), such as saturated stars, also confirmed by the high χ^2 reported in CIGALE.

3.3. AGN Identification

In order to identify the AGNs in our sample, we use the Bayes CIGALE output $f_{\rm AGN}$ (see Section 3.2). Similar to G. Yang et al. (2023; see also E. Durodola et al. 2025; C.-T. Ling et al. 2026), we separate our sources between SF, $f_{\rm AGN} < 0.1$; AGN-mixed, $0.1 \leqslant f_{\rm AGN} < 0.5$; and AGN-dominated, $f_{\rm AGN} \geqslant 0.5$. We identify 1017 SF sources and 502 AGNs (dominated + mixed) in GOODS-N, and 810 SF and 381 AGNs in GOODS-S. We show the distribution of different source types over redshift in Figure 4.

The relative distribution of source types and redshifts is consistent between the two fields, with roughly two-thirds of the population classified as SF and one-third classified as AGN (AGN-mixed and AGN-dominated). The latter will be further used in the AGN luminosity-function (Section 4) calculations and subsequent analysis for quantifying obscuration (Section 5; see also Figure 1). We note that most of the SF sources are present at $z \lesssim 4$, and beyond that the MIRI selection effects preferentially identify mixed and AGN-dominated sources, due to the pronounced hot-dust signatures. This leads to a first statistical sample of 15 high-redshift AGNs ($4.5 \lesssim z \lesssim 6$) that show strong obscuration effects (Section 5; detailed further in G. C. K. Leung et al. 2026).

Although our AGN identification is based on the mid-IR signatures of hot circumnuclear dust, the selection is not intrinsically tied to a particular viewing angle. Provided that the system hosts a detectable hot-dust component, our method should recover the AGN irrespective of orientation, and is therefore sensitive to both obscured and unobscured systems. To verify this explicitly for unobscured sources, we cross-matched our AGN sample with the broad-line AGN identified by JADES in GOODS-N and GOODS-S (I. Juodžbalis et al. 2026), as well as with the optical broad-line AGN in GOODS-S reported by G. P. Szokoly et al. (2004). Compared to the JADES type-1 AGN sample, we recover three of the four sources that lie above our detection limits and within the MEOW footprint: one in GOODS-S and two in GOODS-N. The only exception is GN-73488 from I. Juodžbalis et al. (2026). Upon closer inspection, this source is classified as a little red dot (LRD) in D. D. Kocevski et al. (2025) (UNICORN ID 18850), and is absent from our parent sample because it is not detected in MIRI, consistent with the weak or absent mid-IR emission often reported in LRDs (P. G. Pérez-González et al. 2024a; C. C. Williams et al. 2024; G. C. K. Leung et al. 2025). In addition, we recover all five broad-line AGNs from G. P. Szokoly et al. (2004) that overlap with our footprint. This comparison confirms that our selection does recover known type-1 AGNs when they satisfy the same mid-IR detection criteria applied to the full sample.

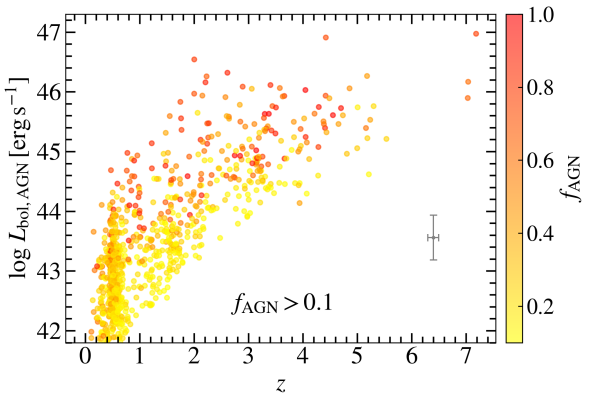


Figure 5. Bolometric AGN luminosity distribution across redshift, color-coded by $f_{\rm AGN}$. We show only sources with $f_{\rm AGN} > 0.1$ (mixed and AGN-dominated), and include typical error bars in gray, corresponding to $|\Delta z| \approx 0.1$ and $|\Delta \log L_{\rm bol}| \approx 0.4$ dex. Overall, the MEOW depth allows us to detect down to $L_{\rm bol} \approx 10^{44}$ erg s^{-1} across cosmic time, and for the identification of high-redshift AGNs up to $z \lesssim 7$, with 18 AGNs at $z \gtrsim 4.5$.

Figure 5 shows the redshift distribution of bolometric luminosity, of the AGN component, for each source with $f_{\rm AGN} > 0.1$. We adopt as bolometric luminosity the CIGALE output bayes.agn.accretion_power, which traces only the intrinsic, unextincted AGN accretion-disk emission, averaged over all viewing directions, and explicitly excludes any stellar or dust emission from the host galaxy. In CIGALE, this quantity is computed as the likelihood-weighted Bayesian mean over the marginalized probability distribution function built from the full grid of fitted SED models. We color-code the points by $f_{\rm AGN}$, finding that luminous AGNs show generally high $f_{\rm AGN}$ and vice versa (see also K. Hamblin et al. 2026; C.-T. Ling et al. 2026).

We note that the three AGNs at $z \gtrsim 7$ are not included in the luminosity-function calculation, as the extremely small number of sources in this regime would make the resulting space-density estimates highly uncertain and sensitive to individual objects. We therefore conservatively restrict the highest-redshift luminosity-function bin to $4.5 \lesssim z \lesssim 6$, where the sample provides a more statistically meaningful constraint.

For the same reason, we do not interpret the apparent gap between $z \approx 5.7$ and $z \approx 7$ as evidence for an intrinsic absence of AGNs but rather as a consequence of the limited survey volume and low expected source counts at these redshifts.

A table with the AGN properties of our entire sample is presented in Appendix A, available in machine-readable form in the online version of the paper.

3.4. Sample Completeness

We assess the completeness of our sample in two components: the photometric detection completeness and the SED-based identification completeness. For the photometric detection completeness, we use source injection simulations. Specifically, we inject sources within a range of F1000W and F2100W fluxes, matched from the AGN templates, and recover them using the same source-detection procedures to calculate the detection completeness in each filter as a function of fluxes. The final detection completeness is the product of the completeness in the two filters at the corresponding fluxes/bolometric luminosities.

We additionally model SED completeness, in order to account for sources that are not recovered as AGN-dominated/AGN-mixed when performing SED fitting. Namely, we define five different redshift bins, used later for the luminosity function (Section 4): $0.5 < z < 1.5$, $1.5 < z < 2.5$, $2.5 < z < 3.5$, $3.5 < z < 4.5$, and $4.5 < z < 6$. We first construct representative AGN-dominated and mixed-source SEDs. For each redshift-luminosity bin, we compute the median SED, separately for AGN-dominated and AGN-mixed populations, normalized at a rest-frame wavelength of 3 μm to mitigate biases driven by intrinsically bright sources. We then scale the median SEDs to a given bolometric luminosity by leveraging the empirical relation between $L_{3\mu\mathrm{m}}$ and L_{bol}, obtained from a linear fit across the full sample.

Using these normalized templates, we generate mock spectra across a grid in redshift and L_{bol} and extract synthetic photometry in the observed filters. To realistically reflect measurement uncertainties, each flux point is perturbed five times using the median photometric error in that filter. Each perturbed mock catalog is then processed through the full CIGALE pipeline. The SED completeness in each redshift-luminosity bin is defined as the fraction of injected AGN or mixed sources that are recovered as $f_{\mathrm{AGN}} > 0.1$ by our selection criteria, relative to the total number of simulated sources. The final completeness is the product of the detection completeness and SED completeness, and the completeness curves are available in G. C. K. Leung et al. (2026).

Finally, we quantify the effective volume for both mixed and AGN sources using the relation

$$V(L_{\mathrm{bol}})_{\mathrm{eff}} = \int \frac{dV}{dz}\, C(L_{\mathrm{bol}}, z)\, dz,$$

where $C(L_{\mathrm{bol}}, z)$ is the combined completeness from source injection and SED completeness, and the final effective volume is the weighted average of the effective volume for mixed and AGN sources in that bin, respectively,

$$V(L_{\mathrm{bol}})_{\mathrm{final}} = \frac{N_{\mathrm{mixed}} V_{\mathrm{eff,mixed}} + N_{\mathrm{AGN}} V_{\mathrm{eff,AGN}}}{N_{\mathrm{mixed}} + N_{\mathrm{AGN}}},$$

where N_{mixed} and N_{AGN} represent the numbers of mixed sources and AGN sources, respectively.

We report the completeness values in the redshift and luminosity bins used for the luminosity-function calculations (Section 4) in Appendix A. The parameter space probed in this study is generally highly complete ($\gtrsim$93%), with the exception of the lowest-luminosity bin at $4.5 < z < 6$, where the completeness decreases to 21% for mixed sources and 11% for AGN-dominated sources; further details will be presented in G. C. K. Leung et al. (2026). Although these points therefore require substantial completeness corrections in the luminosity-function calculation, our main conclusions do not rely on this luminosity range, as it is not covered by the comparison quasar luminosity function (QLF) of G. Kulkarni et al. (2019). Similarly, the second luminosity bin at $4.5 < z < 6$ is only moderately complete, with completeness below 80%, but it is not used in the main obscured-fraction calculations presented in Section 5.

4. Bolometric Luminosity Function

In this section, we discuss the methods employed to infer the AGN luminosity function, in five redshift bins, using both a nonparametric approach as well as a double power-law fit. Subsequently, we will use our luminosity functions in comparison with the existing type-1 UV-bright luminosity functions to quantify obscuration (Section 5; see also Figure 1).

4.1. Nonparametric Approach

Given our final, complete AGN sample (Section 3.4), with associated bolometric luminosities and corresponding uncertainties from the SED fitting (Section 3.2), we can compute the bolometric luminosity function across redshift. We calculate the luminosity functions in five redshift bins, $z = 0.5$–6, using the CIGALE redshift estimates, or spectroscopic redshifts where available (Section 2.5).

First, we calculate the nonparametric luminosity function following the methodology of S. L. Finkelstein et al. (2015, 2023) and G. C. K. Leung et al. (2023). Specifically, we implement a stepwise maximum-likelihood number density in each luminosity bin assuming a Poisson likelihood function. We estimate the uncertainty on the number density using a Markov Chain Monte Carlo (MCMC) approach, without imposing any prior on the number densities. At each iteration of the chain, we randomly draw L_{bol} values, within the uncertainty range, for each object, allowing individual sources to move between luminosity bins as the sampling proceeds. This procedure naturally accounts for both Poisson fluctuations and measurement uncertainties in L_{bol}. The median of the posterior distribution is adopted as the best estimate of the luminosity function, while the 16th and 84th percentiles define the corresponding uncertainty range. The resulting number densities, per dex in bolometric luminosity, are reported in Table 2.

We note that our luminosity function is robust to the main choices made in this study—namely (i) the photometric-redshift choice, CIGALE versus eazy (Section 2.5), and (ii) type-1+type-2 versus type-2 alone CIGALE (Section 3.2). We illustrate these findings in Appendix B. We additionally tested the impact of photometric-redshift uncertainties on the luminosity-function measurements. For sources lacking spectroscopic redshifts, we perturbed the redshift at each step of the MCMC chain using the corresponding CIGALE uncertainty,

Table 2
AGN Bolometric Luminosity Functions in Redshift Bins, along with the Best-fit Parameters for the Double Power-law (Equation [1]), as Well as the Corresponding Completeness Values, $C(L_{\rm bol}, z)$, for Both AGN ($f_{\rm AGN} > 0.5$) and Mixed Sources ($0.1 < f_{\rm AGN} < 0.5$)

Redshift Bin	Luminosity Bin (log)	Completeness (Mixed) %	Completeness (AGN) %	Φ ($\rm Mpc^{-3}\,dex^{-1}$)	Best-fit Params γ_1, $\log\phi_\star$, $\log L_\star$
$0.5 < z < 1.5$	44–44.4	96.92	97.50	$1.87^{+0.51}_{-0.43} \times 10^{-4}$	
	44.4–44.8	97.97	98.02	$1.02^{+0.36}_{-0.29} \times 10^{-4}$	$\gamma_1 = 0.73^{+0.15}_{-0.20}$
	44.8–45.2	98.58	98.58	$5.81^{+2.91}_{-2.14} \times 10^{-5}$	$\log\phi_\star = -4.73^{+0.59}_{-1.31}$
	45.2–45.6	98.58	98.58	$1.44^{+1.55}_{-0.96} \times 10^{-5}$	$\log L_\star = 45.50^{+1.40}_{-0.48}$
	45.6–46	98.58	98.58	$<4.34 \times 10^{-6}$	
$1.5 < z < 2.5$	44–44.4	93.42	93.46	$1.39^{+0.39}_{-0.32} \times 10^{-4}$	
	44.4–44.8	94.28	94.46	$1.04^{+0.30}_{-0.27} \times 10^{-4}$	
	44.8–45.2	95.90	96.17	$5.23^{+2.22}_{-1.77} \times 10^{-5}$	$\gamma_1 = 0.44^{+0.08}_{-0.09}$
	45.2–45.6	97.68	97.51	$4.77^{+2.06}_{-1.53} \times 10^{-5}$	$\log\phi_\star = -5.00^{+0.34}_{-0.46}$
	45.6–46	97.31	98.45	$2.13^{+1.52}_{-1.04} \times 10^{-5}$	$\log L_\star = 46.64^{+0.74}_{-0.43}$
	46–46.4	97.46	98.35	$1.83^{+1.37}_{-0.92} \times 10^{-5}$	
	46.4–46.8	96.97	98.44	$1.01^{+0.97}_{-0.59} \times 10^{-5}$	
$2.5 < z < 3.5$	44.4–44.8	92.52	92.87	$1.45^{+0.37}_{-0.34} \times 10^{-4}$	
	44.8–45.2	93.21	93.29	$1.25^{+0.32}_{-0.29} \times 10^{-4}$	$\gamma_1 = 0.39^{+0.17}_{-0.19}$
	45.2–45.6	93.40	93.77	$8.44^{+2.72}_{-2.42} \times 10^{-5}$	$\log\phi_\star = -4.39^{+0.29}_{-0.50}$
	45.6–46	95.32	95.40	$4.38^{+1.97}_{-1.52} \times 10^{-5}$	$\log L_\star = 46.11^{+0.52}_{-0.26}$
	46–46.4	97.14	96.95	$2.21^{+1.30}_{-1.00} \times 10^{-5}$	
	46.4–46.8	97.88	98.22	$<3.90 \times 10^{-6}$	
$3.5 < z < 4.5$	44.8–45.2	92.26	92.52	$6.44^{+2.99}_{-2.21} \times 10^{-5}$	
	45.2–45.6	92.71	92.94	$6.78^{+2.78}_{-2.24} \times 10^{-5}$	$\gamma_1 = 0.30^{+0.25}_{-0.20}$
	45.6–46	93.20	92.92	$4.79^{+2.34}_{-1.79} \times 10^{-5}$	$\log\phi_\star = -4.50^{+0.23}_{-0.40}$
	46–46.4	93.91	93.59	$1.93^{+1.48}_{-1.02} \times 10^{-5}$	$\log L_\star = 46.20^{+0.39}_{-0.25}$
	46.4–46.8	96.25	94.56	$<4.84 \times 10^{-6}$	
$4.5 < z < 6$	44.2–44.9	21.05	11.94	$2.50^{+2.69}_{-1.65} \times 10^{-5}$	
	44.9–45.6	78.45	73.51	$2.05^{+1.10}_{-0.87} \times 10^{-5}$	$\gamma_1 = 0.22^{+0.23}_{-0.15}$
	45.6–46.3	92.55	92.67	$1.77^{+0.90}_{-0.68} \times 10^{-5}$	$\log\phi_\star = -4.99^{+0.37}_{-0.56}$
	46.3–47.0	93.76	93.15	$<3.15 \times 10^{-6}$	$\log L_\star = 46.40^{+0.62}_{-0.44}$

Note. The luminosity-function values reported in this table already include the completeness corrections.

and rescaled the bolometric luminosity according to the change in luminosity distance squared. We find that the resulting luminosity functions are robust to these perturbations, with negligible differences and no measurable impact on the inferred obscured fractions.

4.2. Parametric Approach

To ensure continuous bolometric luminosity coverage in our luminosity function, necessary for meaningful comparison with existing literature (Section 5), we also fit our results with a double power law, following standard practice,

$$\phi(L) = \frac{dn}{d\log L} = \frac{\phi_*}{(L/L_*)^{\gamma_1} + (L/L_*)^{\gamma_2}}, \quad (1)$$

where ϕ_* is the comoving number density normalization, L_* is the break luminosity, and γ_1 and γ_2 are the faint-end and bright-end slopes, respectively.

Therefore, there are four free parameters in Equation (1). However, given the limited data at the bright end ($L_{\rm bol} \gtrsim 10^{47}\,\rm erg\,s^{-1}$; Figure 5), we fix the bright-end slope, γ_2, to the value reported in M. Lacy et al. (2015), $\gamma_2 = 2.48$. This choice is well motivated, as M. Lacy et al. (2015) employed a similar AGN selection function but extended to higher luminosities owing to their larger survey area. A caveat of this approach, however, is the lack of high-redshift ($z \gtrsim 3$) constraints. Nevertheless, M. Lacy et al. (2015) found no significant redshift evolution in the bright-end slope, and their γ_2 values are consistent with those of X. Shen et al. (2020) at high redshift, who fit a more homogeneous AGN sample. Adopting the M. Lacy et al. (2015) value for γ_2 is thus a reasonable choice, and we note that modest deviations from this value have negligible impact on our results, as the luminosity function is primarily constrained by the more numerous, lower-luminosity AGNs ($L_{\rm bol} \lesssim 10^{47}\,\rm erg\,s^{-1}$) that dominate our sample.

For the fit, we follow a similar approach to S. L. Finkelstein et al. (2015). Namely, we compute the likelihood that the number of observed AGNs in a given luminosity bin is equal to the predicted number for a given set of parameters. Instead of performing a grid-based search, we use MCMC to span the parameter space and compute the uncertainties in the three parameters we fit. We use the same luminosity bins as in Section 4.1 (see also Table 2). We model the probability distribution as Poissonian, due to the small-number statistics regime of our sample. For each redshift bin, we perform 10 independent MCMC chains, with 10,000 steps each.

Lastly, we report our results from both the parametric and the nonparametric approach in Table 2.

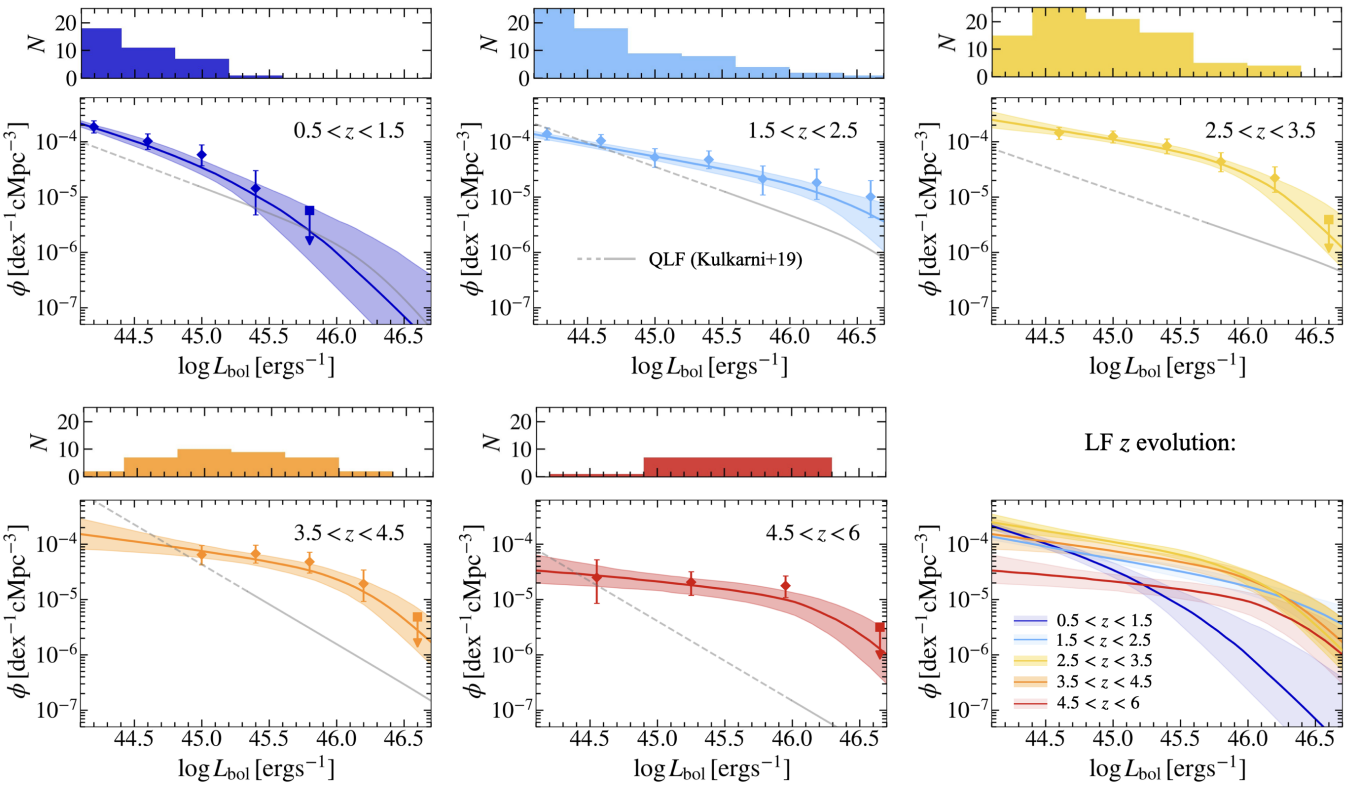


Figure 6. AGN luminosity functions, along with the double power-law fits, color-coded by redshift. The shaded regions represent the 16th–84th percentile of the MCMC chains (see Section 4.2). For comparison, we show the luminous type-1 QLF from G. Kulkarni et al. (2019), in gray, with the solid line representing the fits to the data and the dashed line representing the extrapolations. We also show the AGN luminosity distributions in the histograms. We further quantify the excess of obscured AGNs in our sample in Figure 7.

5. Results

In this section, we use the luminosity functions described in Section 4 to quantify the obscured-AGN population missed by optical/UV studies. We first qualitatively show how our luminosity function, including both obscured and unobscured sources, compares with the type-1 UV-bright QLF reported in G. Kulkarni et al. (2019). To estimate the obscured-AGN fraction in each luminosity and redshift bin (Section 5.2), we integrate our MEOW/mid-IR luminosity function to determine the total AGN abundance (obscured + unobscured), and independently integrate the QLF for the unobscured population (see also Figure 1).

5.1. Luminosity Functions: MEOW AGN versus Type-1 Quasars

We show both the nonparametric luminosity function (Section 4.1) and the double power-law fits (Section 4.2), along with the corresponding uncertainties, in Figure 6. To illustrate the redshift evolution more clearly, we combine all luminosity functions in the bottom-right panel of Figure 6. We notice a smooth luminosity-function evolution between our redshift bins, with overall small uncertainties, apart from the high-luminosity end, due to small number statistics. In the lowest-redshift bin, $0.5 < z < 1.5$, the luminosity function declines steeply at the bright end. By contrast, the higher-redshift luminosity functions turn over at higher luminosities, indicating a relatively larger abundance of luminous AGNs. At lower luminosities, the luminosity functions become progressively flatter with increasing redshift, while the $4.5 < z < 6$ bin shows a substantially lower normalization. However, this low-luminosity regime is strongly affected by incompleteness (Section 3.4).

We compare our results to the "Model 1" QLF reported in G. Kulkarni et al. (2019), computed at the median redshift in each of our five redshift bins. The G. Kulkarni et al. (2019) sample consists exclusively of spectroscopically confirmed, UV-bright type-1 quasars extending to $z \lesssim 6$, making it well suited for estimating the obscured fractions of our mid-IR-selected AGNs (see also Section 6.1). We note that the QLF in G. Kulkarni et al. (2019) is originally reported in UV magnitudes, M_{1450}, which we convert to bolometric luminosity using the best fit of the J. C. Runnoe et al. (2012) relation. The uncertainties in the conversion introduce an additional source of error into our results that cannot be explicitly accounted for, but are expected to be subdominant at the population level.

Overall, our results lie above the type-1 UV-bright QLF reported in G. Kulkarni et al. (2019), in the regions with data coverage in G. Kulkarni et al. (2019) (i.e., not extrapolated). The excess of moderately luminous AGNs in our sample suggests a substantial contribution from obscured growth that is not captured in UV-bright quasar surveys, which we will quantify in the next subsection. The accompanying number-count histograms reinforce this picture: While the bright end remains sparsely populated, a significant population of lower-luminosity AGNs is detected out to $z \approx 6$, with a much higher abundance than the type-1 UV-bright quasars. Taken together, these results highlight the importance of mid-IR selection for tracing the full demographic of black hole growth across

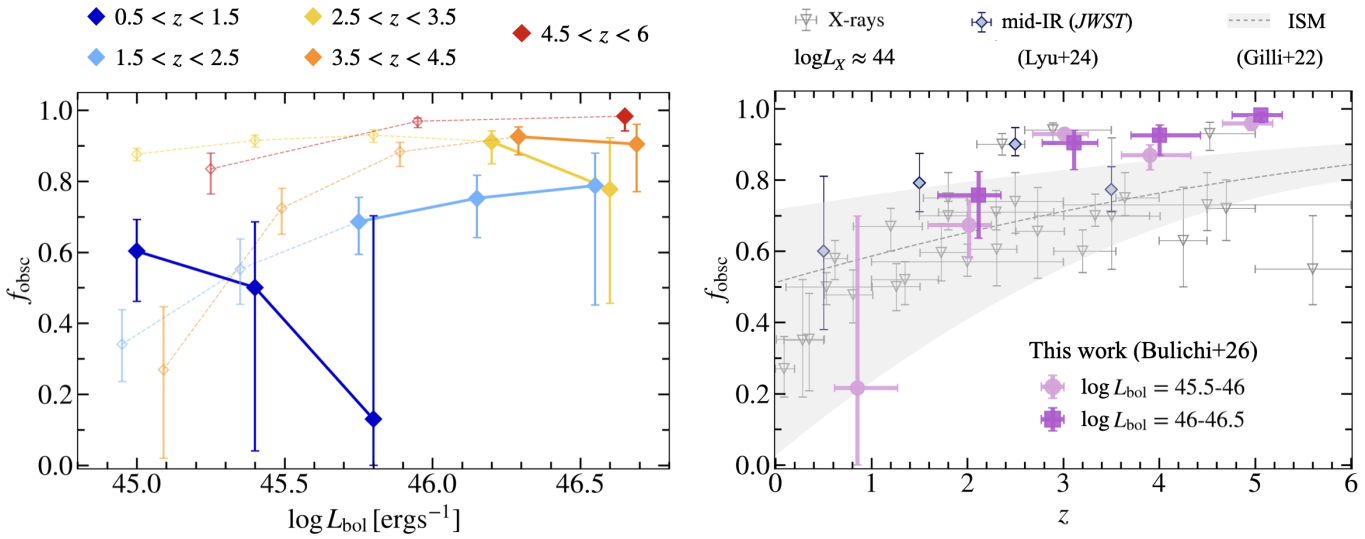


Figure 7. Obscured fraction as function of luminosity, in five redshift bins (left), and as a function of redshift (right). On the left, we show the results that come from QLF extrapolations (see Figure 6) as empty points, connected by dashed lines, and the rest of the data as solid points connected by solid lines. We color-code the data by redshift, and use the same luminosity bins as in Figure 6. On the right, we show the redshift evolution across our faint sample (log $L_{\rm bol}$ = 45.5–46 erg s^{-1}; light purple) and bright sample (log $L_{\rm bol}$ = 46–46.5 erg s^{-1}; dark purple). The horizontal error bars indicate the 16th–84th percentile of the redshift distributions for the sources in each redshift bin. We overplot the X-ray constraints from D. Burlon et al. (2011), K. Iwasawa et al. (2012), Y. Ueda et al. (2014), J. Buchner et al. (2015), T. Liu et al. (2017), L. Zappacosta et al. (2018), F. Vito et al. (2018), K. Iwasawa et al. (2020), A. Peca et al. (2023), E. Pouliasis et al. (2024), and C. L. Barlow-Hall & J. Aird (2025), with 2–10 keV luminosities log $L_X \approx 44$ ergs^{-1} as gray points; the Atacama Large Millimeter/submillimeter Array (ALMA) constraints on $f_{\rm obsc}$ from the ISM column density (R. Gilli et al. 2022) as the gray band, with the dashed line showing the median predictions; as well as early JWST results (J. Lyu et al. 2024) as blue diamonds, indicating the optically obscured AGNs in their sample.

cosmic time, especially in regimes where dust obscuration is expected to be common (see also Section 6.2)

5.2. Obscured Fraction

We quantify the obscured fraction using the luminosity functions of our MEOW sample, compared to the type-1 UV-bright QLF reported in G. Kulkarni et al. (2019) (see Section 5.1). Specifically, we define the obscured fraction as the abundance of obscured sources over the total AGN number density,

$$f_{\rm obsc} = \frac{n_{\rm obsc}}{n_{\rm tot}} = 1 - \frac{n_{\rm unobsc}}{n_{\rm tot}},$$

where $n_{\rm unobsc} = \int \phi_{\rm QLF}(L),\ dL$ is the number density of unobscured, UV-bright type-1 AGNs, obtained by integrating the luminosity function from G. Kulkarni et al. (2019). In contrast, $n_{\rm tot} = \int \phi_{\rm MIR}(L),\ dL$ is the total AGN number density, obtained by integrating our mid-IR parametric luminosity function (Section 4.2; see also Figure 1).[17] This total includes both obscured and unobscured AGNs, since the MEOW selection is sensitive to hot-dust emission irrespective of orientation, as demonstrated in Section 3.3.

As discussed further in Section 6.1, we adopt the G. Kulkarni et al. (2019) QLF as the most appropriate comparison for this study, as it specifically represents UV-bright, type-1 AGNs/quasars and provides reasonable coverage across the redshift and luminosity ranges probed here. Generally, the low-luminosity regimes (i.e., $L_{\rm bol} < 10^{45}$ erg s^{-1}) do not overlap with our data, as indicated by the dashed lines in Figure 6; however, we do not draw conclusions from the obscured fractions inferred in these regimes. Likewise, as discussed in Section 3.4, our low-luminosity measurements in the highest-redshift bins are strongly affected by completeness corrections and fall in a luminosity range not covered by G. Kulkarni et al. (2019). We therefore exclude these measurements from the final obscured-fraction calculations.

We show the obscured-fraction evolution as a function of luminosity, for each redshift bin, as well as a function of redshift in Figure 7. We denote the results coming from the extrapolation in the G. Kulkarni et al. (2019) QLF with a dashed line, and empty points, and the rest with solid points connected by solid lines. We estimate the uncertainties by sampling the luminosity-function MCMC chains (Section 4.2) and computing the 16th–84th percentile range of the resulting obscured fractions.

The obscured-AGN fraction ($f_{\rm obsc}$) in the MEOW sample displays a tentative luminosity dependence at low redshift, with the lowest-redshift bin hinting at decreasing obscuration toward higher luminosities, albeit not statistically significant, due to the large uncertainties. This tentative behavior is broadly consistent with a "receding torus" model (e.g., A. Lawrence 1991; C. Simpson 2005; R. Gilli et al. 2007; E. Lusso et al. 2013), which predicts that the high luminosities reduce the dust-covering factor. However, the trend reverses in the higher-redshift bins, hinting at an evolving obscuration scenario (e.g., D. B. Sanders et al. 1988; P. F. Hopkins et al. 2008; see Section 6.2).

We additionally notice an increase in obscuration with redshift for the luminosity ranges covered by the G. Kulkarni et al. (2019) QLF, explored further in the right panel of Figure 7 and also included in Table 3. We split our sources in two luminosity bins: log$L_{\rm bol}$ = 45.5 − 46 erg s^{-1} and log$L_{\rm bol}$ = 46 − 46.5 erg s^{-1}, to differentiate between fainter and brighter sources while maintaining comparable luminosity

[17] Throughout this study, our inferred obscured fractions refer strictly to UV obscuration (i.e., the fraction of AGNs missed by UV selection).

Table 3
Obscured Fractions in Redshift Bins, Split in Two Luminosity Ranges, $\log L_{\rm bol} = 45.5 - 46$ [erg s^{-1}] (faint) and $\log L_{\rm bol} = 46 - 46.5$ [erg s^{-1}] (bright), for All Three Models of G. Kulkarni et al. (2019): Model 1 (fiducial), Shown in the Right Panel of Figure 7, as Well as Models 2 and 3

Redshift Bin	$f_{\rm obsc}$ (faint) $\log L_{\rm bol} = 45.5 - 46$	$f_{\rm obsc}$ (bright) $\log L_{\rm bol} = 46 - 46.5$
$0.5 < z < 1.5$	$0.216^{+0.482}_{-0.216}$ **(fiducial)**	⋯
	K19 Model 2: $0.213^{+0.484}_{-0.213}$	⋯
	K19 Model 3: $0.216^{+0.483}_{-0.216}$	⋯
$1.5 < z < 2.5$	$0.673^{+0.070}_{-0.092}$ **(fiducial)**	$0.757^{+0.066}_{-0.120}$ **(fiducial)**
	K19 Model 2: $0.640^{+0.077}_{-0.102}$	$0.755^{+0.067}_{-0.121}$
	K19 Model 3: $0.663^{+0.072}_{-0.096}$	$0.767^{+0.064}_{-0.115}$
$2.5 < z < 3.5$	$0.929^{+0.013}_{-0.019}$ **(fiducial)**	$0.904^{+0.034}_{-0.076}$ **(fiducial)**
	K19 Model 2: $0.764^{+0.046}_{-0.066}$	$0.823^{+0.064}_{-0.141}$
	K19 Model 3: $0.904^{+0.019}_{-0.027}$	$0.896^{+0.038}_{-0.083}$
$3.5 < z < 4.5$	$0.870^{+0.028}_{-0.043}$ **(fiducial)**	$0.926^{+0.028}_{-0.057}$ **(fiducial)**
	K19 Model 2: $0.931^{+0.015}_{-0.022}$	$0.958^{+0.016}_{-0.032}$
	K19 Model 3: $0.969^{+0.007}_{-0.010}$	$0.974^{+0.010}_{-0.020}$
$4.5 < z < 6$	$0.958^{+0.012}_{-0.020}$ **(fiducial)**	$0.983^{+0.007}_{-0.022}$ **(fiducial)**
	K19 Model 2: $0.974^{+0.007}_{-0.012}$	$0.989^{+0.005}_{-0.014}$
	K19 Model 3: $0.985^{+0.004}_{-0.007}$	$0.992^{+0.003}_{-0.010}$

coverage with the UV-bright quasars in G. Kulkarni et al. (2019), as well as meaningful comparisons with X-ray studies (D. Burlon et al. 2011; K. Iwasawa et al. 2012; Y. Ueda et al. 2014; J. Buchner et al. 2015; T. Liu et al. 2017; L. Zappacosta et al. 2018; F. Vito et al. 2018; K. Iwasawa et al. 2020; E. Pouliasis et al. 2024; C. L. Barlow-Hall & J. Aird 2025).

The redshift evolution we find aligns qualitatively with X-ray studies, but our mid-IR selection generally identifies an even larger proportion of highly obscured systems and is above the indirect ISM constraints from R. Gilli et al. (2022) at high redshift. When compared to the early JWST results of J. Lyu et al. (2024), we find similarly high levels of optical obscuration over the overlapping redshift range. These results suggest that much of the black hole growth (up to 98–99%) is deeply embedded, with heavy dust columns capable of concealing luminous accretion from optical and even hard X-ray surveys (see also Section 6.2).

6. Discussion

In this section, we provide a detailed interpretation of the results presented in Section 5. We first compare our findings with previously reported luminosity functions (Section 6.1) and motivate our choice of the QLF used in the obscured-fraction calculations (Section 5.2). We then place our sample in the context of prior multiwavelength studies, as well as existing literature models, highlighting the newly identified obscured AGNs uncovered in this work (Section 6.2). Finally, we interpret the inferred obscured fractions in the broader context of SMBH growth (Section 6.3).

6.1. Choice of QLF

While the luminosity function is a powerful probe of structure formation and evolution (D. Roberts et al. 2026), its accuracy is still strongly limited by selection effects. As such, the findings of this study are highly sensitive to the comparison

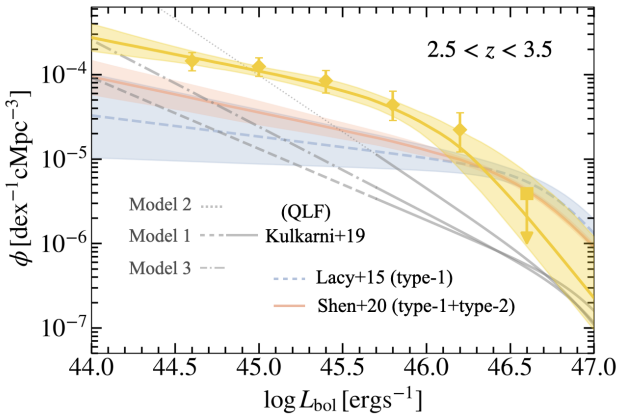


Figure 8. AGN luminosity function, for our third redshift bin, $2.5 < z < 3.5$, in comparison with previous literature results. For all the QLFs shown, we use the value at the median redshift in our distribution, and the shaded regions represent the errors in the fitting. The solid-dashed line is the G. Kulkarni et al. (2019) model, the same as in Figure 6, and we additionally plot the other two models reported in G. Kulkarni et al. (2019), which account for different selection effects (see text), as well as the QLFs reported in M. Lacy et al. (2015) (type-1) and X. Shen et al. (2020) (type-1 + type-2). Using the same convention as in Figure 6, the dashed lines show the regions where the luminosity functions are extrapolated.

with the QLF used for the $f_{\rm obsc}$ calculations (Section 5.2). Here we investigate all models for the UV-selected QLFs reported in G. Kulkarni et al. (2019), along with the results from the mid-IR selected AGNs in M. Lacy et al. (2015) and the multiwavelength (IR-to-X-ray) sample of X. Shen et al. (2020), and show all of these results in Figure 8, at $2.5 < z < 3.5$, $z_{\rm med} = 3.06$.

G. Kulkarni et al. (2019) provide robust redshift and completeness estimates, applying homogeneous assumptions for the cosmology and the intrinsic AGN SED, addressing the large methodological scatter present in preceding work. We already showed Model 1 in Section 4, which contains all the datasets compiled in the paper and models the faint-end slope as a double power law. Their Model 2 excludes the results with only approximate selection functions, while Model 3 further modifies the faint-end slope as a linear fit in $(1 + z)$. Although these models show reasonable agreement where data exist, they diverge significantly toward the low-luminosity regime at high redshift, where there are no observational data points. We decided to use Model 1 as the baseline of this work, as it is the most complete, but note that the results are sensitive to this choice, especially in the extrapolated regions, and thus the systematic uncertainties in the low-luminosity regime are much higher than the luminosity-function fitting uncertainties detailed in Table 3. We therefore do not draw conclusions in luminosity ranges where the fits from G. Kulkarni et al. (2019) are extrapolated. In the luminosity ranges directly covered by the G. Kulkarni et al. (2019) data, we report the corresponding obscured fractions for Models 2 and 3 in Table 3. Overall, the results from the three models agree within 1σ, with the exception of the $2.5 < z < 3.5$ bin, where the G. Kulkarni et al. (2019) models differ most substantially, as also shown in Figure 8. While we consider Model 1 to be the most suitable choice for this work, we caution that the obscured fraction at $z \approx 3$ is sensitive to this model choice, as reflected in Table 3. The results in the other redshift bins remain robust for this assumption.

M. Lacy et al. (2015) selects the AGN sample in mid-IR with Spitzer, similar to this work. Using spectroscopic follow-up, they differentiate between type-1 and type-2 based on the broad emission lines: Objects with a broad component are classified as type-1. While the initial selection effects are similar to those used in this paper, the M. Lacy et al. (2015) fits are limited in redshift $z \lesssim 3$ and luminosity $L_{\rm bol} \gtrsim 10^{47}$ erg s^{-1}, thus not overlapping with the data in our sample. Thus we did not use the M. Lacy et al. (2015) type-1 luminosity function to quantify obscuration, but note that their results predict larger ϕ values than G. Kulkarni et al. (2019). We speculate that this might result from the small number statistics in M. Lacy et al. (2015), as the number of sources is significantly lower than in G. Kulkarni et al. (2019), as well as the different classifications as type-1. We, however, use the M. Lacy et al. (2015) results for the bright-end luminosity-function constraints (Section 4.2), as their methodology for the whole AGN population (type-1 + type-2) aligns closely with ours.

Lastly, while X. Shen et al. (2020) include both obscured and unobscured AGNs, their high-redshift obscured population is dominated by X-ray-selected sources. As a result, this sample may be affected by survey incompleteness, uncertainties in X-ray-to-UV bolometric corrections, and biases against Compton-thick AGNs. Consequently, X. Shen et al. (2020) exhibit a behavior similar to M. Lacy et al. (2015) at high redshift, where only a small fraction of obscured AGNs are represented. The fact that our luminosity function lies above that of X. Shen et al. (2020) underscores the effectiveness of mid-IR selection in identifying obscured AGNs that are otherwise missed in UV and X-ray surveys, an effect that is particularly pronounced at lower luminosities ($L_{\rm bol} \lesssim 10^{46}$ erg s^{-1}). We note, however, that at lower redshift, our luminosity function shows good agreement with X. Shen et al. (2020), where the inclusion of mid-IR-selected AGNs in X. Shen et al. (2020) leads to a more complete census of both obscured and unobscured populations.

We further quantify the missing obscured AGNs compared to previous results and models in the next subsection, and conclude by discussing the implications of our inferred obscured fraction to early SMBH growth (Section 6.3).

6.2. Comparison with Literature AGN Samples

As shown in Figure 7, our inferred obscured fractions are generally higher than those derived from X-ray studies, at high redshift. This discrepancy can be partly attributed to the different methodology used to infer $f_{\rm obsc}$ in this work compared to X-ray-based analyses. However, an additional contributor is the presence of X-ray-weak AGNs in our sample, potentially arising from high dust-covering fractions and/or large column densities (i.e., Compton-thick AGNs). To investigate this scenario, we compare our luminosity functions with the luminosity functions of X-ray-selected AGNs, reported in F. Vito et al. (2014) and Y. Ueda et al. (2014), in Figure 9, using their "luminosity-dependent density evolution" fit at the median redshift of our sample in each redshift bin. We include both X-ray-selected AGN luminosity functions because they probe complementary redshift and luminosity regimes, together providing the closest comparison to the parameter space covered by our sample. In both cases, the conversion between the X-ray luminosity $L_{2-10\,\rm keV}$ and bolometric luminosity was done using the relation reported in P. F. Hopkins et al. (2007) and applying the corresponding transformation to the luminosity function.

In the first two redshift bins, our luminosity functions agree, within the uncertainties, with the corresponding X-ray-selected AGN luminosity functions. This is consistent with the agreement between our inferred obscured fractions and those derived from X-ray studies over the same redshift range (Figure 7), suggesting that at $z \lesssim 3$, X-ray luminosity functions are less strongly affected by incompleteness and recover a substantial fraction of the underlying AGN population (e.g., X. Guo et al. 2026; G. Mazzolari et al. 2026). At higher redshifts, however, our mid-IR selection identifies additional AGNs that are not detected in X-rays, pointing to a population of highly obscured systems and/or sources with large gas columns that may not be fully accounted for in current X-ray selections. This is also reflected in our systematically higher obscured fractions relative to X-ray-based estimates at $z \gtrsim 3$ (Figure 7).

Compared to early JWST results (J. Lyu et al. 2024), we adopt a different definition to quantify obscuration. In J. Lyu et al. (2024), obscuration is characterized through the AGN contribution to the total emission in the rest-frame 1–10 μm range, which, within the CIGALE SED-fitting framework implemented in this study, is strongly degenerate with the emission from the stellar component. As a result, a strictly direct comparison between the two approaches is not possible. Nevertheless, we find overall consistency with the obscuration levels reported in J. Lyu et al. (2024). We additionally cross-match our sample with the AGN identified by J. Lyu et al. (2024), finding good overlap in the luminosity regimes probed by both studies: Of the 90 SMILES sources above the MEOW detection limits, we recover 84. The six unrecovered sources are missed due either to the lack of F444W coverage, in two cases, or to differences in the deblending, in the remaining four. Since the latter effect is included in our completeness simulations, it is not expected to introduce systematic uncertainties in the luminosity function or obscured-fraction measurements. We discuss further the implications of this comparison in Appendix C.

We also find that our inferred obscured fractions show a mild dependence on luminosity and a strong redshift dependence. In the lowest-redshift bin, $0.5 < z < 1.5$, the obscured fraction goes down with luminosity, in agreement with "receding torus" models (A. Lawrence 1991; C. Simpson 2005; R. Gilli et al. 2007; E. Lusso et al. 2013), which predict that higher luminosities drive the inner radius of the torus outward, thereby reducing the dust-covering fraction. At higher redshifts, however, we notice the opposite trend, with the caveat that this is mainly driven by the regions where the G. Kulkarni et al. (2019) QLF is extrapolated. This is in agreement with previous Spitzer mid-IR studies (e.g., M. Lacy et al. 2015), which support evolutionary scenarios proposed by, e.g., D. B. Sanders et al. (1988) and P. F. Hopkins et al. (2008), in which quasars begin their activity in highly obscured environments. This is also supported by the increase in obscuration with redshift shown in Figure 7, which agrees with earlier work in X-ray surveys (e.g., E. Treister & C. M. Urry 2006; T. Liu et al. 2017). However, X-ray studies suggest that at higher redshifts, obscuration is dominated by dust distributed on galactic scales rather than by the compact, hot torus traditionally invoked in AGN unification models (e.g., R. Gilli et al. 2022; B. Trefoloni et al. 2025). In contrast,

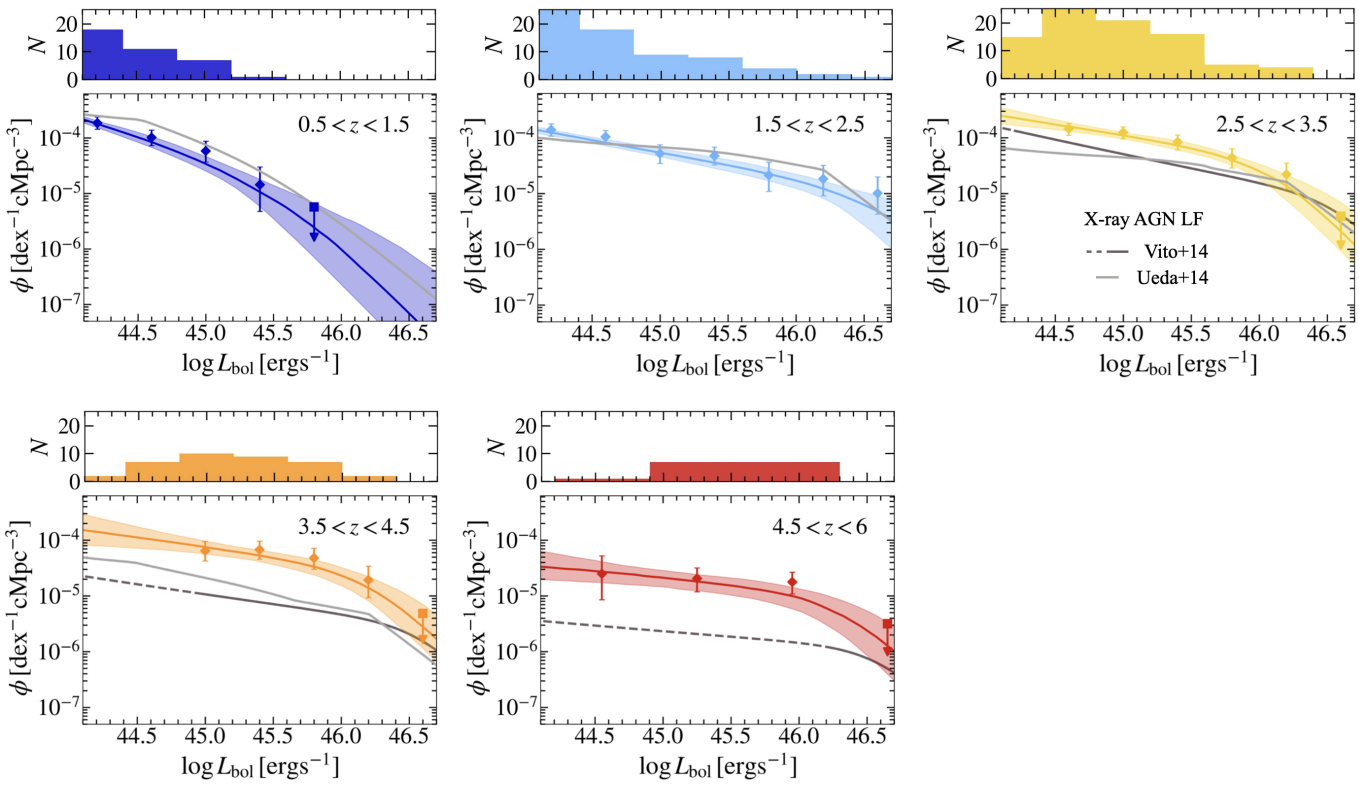


Figure 9. Comparison of the bolometric AGN luminosity function for MEOW-selected AGNs (colored lines with shaded regions) and X-ray-selected AGNs (gray lines, from Y. Ueda et al. 2014 and F. Vito et al. 2014). Similar to Figure 6, the dashed lines mark the luminosity range where the luminosity functions are extrapolated. At low redshift ($z < 3$), our luminosity functions agree well with those inferred from X-ray-selected AGNs. At $z \gtrsim 3$, the higher AGN abundance compared to the X-ray-selected AGN luminosity functions suggests the existence of an additional, heavily obscured AGN population not captured by X-ray surveys, with the excess increasing toward higher redshift.

we still notice a significant increase in obscuration with our MIRI-based analysis that primarily traces hot-dust emission associated with AGN heating. This apparent contradiction may arise because many previous X-ray constraints were derived from lower-redshift samples ($z \lesssim 2$), where the physical conditions and dominant obscuration mechanisms could differ. Second, while the hot dust we detect is consistent with AGN heating, it does not necessarily require a classical torus geometry; it may instead originate from dust distributed more broadly, provided it is sufficiently heated by the central engine. Lastly, the rest-frame near-infrared emission from the hot torus will better penetrate the galaxy dust than the rest-UV and optical emission, making it a useful tracer in either case of obscuration (see e.g., J. D. Silverman et al. 2023).

Finally, we caution that the systematic uncertainties, especially due to the choice of the QLF, might be underestimated, thus affecting some obscured-fraction estimates, predominantly at the low-luminosity end (see Section 5.1). However, the high-luminosity end constraints from G. Kulkarni et al. (2019) converge to similar values, making the $f_{\rm obsc}$ estimations more robust in this regime. This strengthens our confidence in the obscured fraction at high redshift and high luminosity, discussed in more detail in the next subsection.

6.3. Implications for SMBH Growth

As detailed in, e.g., A.-C. Eilers et al. (2018, 2024), the short UV-bright lifetimes inferred independently from ionizing signatures, i.e., proximity zones, Lyα nebulae and damping wings measurements (A.-C. Eilers et al. 2017, 2018; F. B. Davies et al. 2019; I. T. Andika et al. 2020; A.-C. Eilers et al. 2020; K. A. Morey et al. 2021; S. Satyavolu et al. 2023; D. Ďurovčíková et al. 2024, 2025), as well as population-study duty cycles (J. Arita et al. 2023; A.-C. Eilers et al. 2024; E. Pizzati et al. 2024; J. Huang et al. 2026; J.-T. Schindler et al. 2026), can be alleviated if the early SMBH growth occurs in heavily dust-enshrouded environments that suppress the ionizing UV emission.

The results of our study point toward high obscured fractions, as high as $f_{\rm obsc} \approx 98$–99% in the highest-redshift bin at $4.5 < z < 6$ (Table 3). This could alleviate some of the tension raised by the short UV-luminous duty cycles of order $\sim$0.1–1% reported by recent studies at $z \gtrsim 6$ (A.-C. Eilers et al. 2024; E. Pizzati et al. 2024; J. Huang et al. 2026; J.-T. Schindler et al. 2026), as it implies that there is a large fraction of accreting obscured black holes. We caution, however, that duty-cycle studies generally probe higher luminosities ($L_{\rm bol} \approx 10^{47}\,{\rm erg\,s^{-1}}$) and higher redshifts ($z \gtrsim 6$) than those considered in this work. A direct comparison is therefore not currently possible. In the future, however, as more photometric and spectroscopic JWST datasets become available (e.g., JWST #6827), it will be possible to quantify the clustering and duty cycles of both obscured and unobscured AGNs over a common $L_{\rm bol}$–z parameter space, providing a more complete view of SMBH growth. At present, our results suggest that the high obscured fractions inferred at $z \approx 5$ and $L_{\rm bol} \approx 10^{45}$–$10^{46}\,{\rm erg\,s^{-1}}$ can help reconcile rapid SMBH growth, with up to $\sim$98–99% of accretion occurring in dust-enshrouded phases missed by traditional optical/UV surveys. If similarly high obscured

fractions persist at $z \gtrsim 6$ and at higher luminosities, they would provide an important pathway for explaining the rapid assembly of early SMBHs, despite the short luminous/quasar phases.

7. Conclusions

We have presented a measurement of the obscured-AGN fraction from $0.5 \lesssim z \lesssim 6$ based on the JWST/MIRI MEOW sample in the two GOODS fields. Using full SED fitting to identify the AGNs and to infer their bolometric luminosities, we construct luminosity functions of the mid-IR-selected AGNs in five redshift bins and compare these to the type-1 UV-bright QLF from G. Kulkarni et al. (2019).

Our results reveal a substantial population of dust-enshrouded AGNs at early cosmic times. In particular, at high redshift ($z \gtrsim 4.5$) and high luminosity ($\log L_{\rm bol} \gtrsim 46$ erg s^{-1}), the estimated obscured-fraction approaches ∼98–99%. While the detailed luminosity dependence of the obscured fraction remains sensitive to the choice of type-1 QLF at the faint end, the high-luminosity regime is comparatively well constrained, suggesting that the black hole accretion timescales could be up to 2 orders of magnitude larger than previous estimates based on proximity zones and clustering of UV-luminous quasars. Future measurements of quasar lifetimes from damping-wing signatures in faint quasars (JWST #9180, PI: J. F. Hennawi) and from clustering analyses (JWST #7519, PI: J. Arita) will be key to further constraining this interpretation.

Our estimates of the obscured-AGN fraction exceed those derived in previous studies from X-ray-selected samples at $z \gtrsim 3$. This suggests that a significant fraction of SMBH growth at early times occurs in heavily dust-embedded environments, with a significant population of heavily obscured/Compton-thick AGNs missed by X-ray selections toward higher redshifts.

Overall, these results highlight the indispensable role of mid-IR selection in constructing a complete census of SMBH growth at high redshift. Future spectroscopic follow-up, alongside wider and deeper MIRI surveys, will be key to refining obscuration estimates and uncovering the physical conditions and environments that regulate early, dust-rich black hole growth. With forthcoming data from programs such as JWST #6827 (PI: A.-C. Eilers), this work will serve as an important benchmark for placing tighter constraints on early SMBH assembly and for testing evolutionary scenarios in which black hole growth progresses from a heavily obscured phase to a later, more unobscured state.

Acknowledgments

The authors would like to thank the referee for a very constructive report that helped improve the clarity of the paper. We also thank Allison Kirkpatrick, Giovanni Mazzolari, Dominika Ďurovčíková, Megan Masterson, John Silverman, Erini Lambrides, and Johannes Buchner for helpful discussions. T.-E.B. and G.C.K.L. acknowledge support from NASA through STScI award JWST-GO-5407. Support for program #5407 was provided by NASA through a grant from the Space Telescope Science Institute, which is operated by the Association of Universities for Research in Astronomy, Inc., under NASA contract NAS 5-03127. This work is based on observations made with the NASA/ESA/CSA James Webb Space Telescope. The data were obtained from the Mikulski Archive for Space Telescopes at the Space Telescope Science Institute (doi:10.17909/twrw-zw46), which is operated by the Association of Universities for Research in Astronomy, Inc., under NASA contract NAS 5-03127 for JWST. P.G.P.-G. acknowledges support from grant PID2022-139567NB-I00, funded by Spanish Ministerio de Ciencia, Innovación y Universidades MCIU/AEI/10.13039/501100011033, FEDER *Una manera de hacer Europa*.

Software: astropy (Astropy Collaboration et al. 2013, 2018, 2022), eazy (G. B. Brammer et al. 2008), SExtractor (E. Bertin & S. Arnouts 1996), Matplotlib (J. D. Hunter 2007), NumPy (C. R. Harris et al. 2020), SciPy (P. Virtanen et al. 2020), JWST Calibration Pipeline (H. Bushouse et al. 2022).

Appendix A
Tabulated Data

We provide the IDs, coordinates, and physical properties of our AGN sample ($f_{\rm AGN} > 0.1$) in Table A1, available in its entirety in machine-readable form in the online version of the paper.

Table A1
Properties of all AGNs Identified in the MEOW Sample

NIRCam ID	R.A. (deg)	Decl. (deg)	z	$z_{\rm type}$	$f_{\rm AGN}$	$\log L_{\rm bol}$ (erg s^{-1})
104301	189.354997	62.241363	0.1046	phot	$0.90^{+0.02}_{-0.02}$	$41.07^{+0.04}_{-0.05}$
103521	189.354893	62.250678	0.4577	spec	$0.32^{+0.10}_{-0.10}$	$42.35^{+0.13}_{-0.19}$
17959	189.213667	62.181003	1.2258	spec	$0.83^{+0.11}_{-0.11}$	$44.72^{+0.07}_{-0.08}$
6281	189.184761	62.248055	1.4870	spec	$0.32^{+0.13}_{-0.13}$	$44.84^{+0.16}_{-0.26}$
7843	189.205762	62.238238	3.1934	phot	$0.52^{+0.16}_{-0.16}$	$45.22^{+0.11}_{-0.15}$

(This table is available in its entirety in machine-readable form in the online article.)

Appendix B
Luminosity-function Dependence on Modeling Choices

Figure B1 presents the nonparametric luminosity function and the corresponding number counts in each luminosity bin for $2.5 < z < 3.5$. The yellow diamonds show the fiducial luminosity function adopted in this work: Spectroscopic redshifts are fixed for the 19 sources where they are available, while photometric redshifts for the remaining objects are derived with `CIGALE`. The squares follow the same treatment, again fixing the 19 spectroscopic redshifts, but compute the photometric redshifts with `eazy` for the rest. Although a few sources shift between luminosity bins—most noticeably at the low-luminosity end—the overall luminosity function remains robust to the choice of the photo-z method, with all measurements consistent within the 1σ uncertainties.

The circles show the luminosity function obtained when fitting both type-1 and type-2 AGNs, rather than the fiducial type-2 only approach used throughout the main paper. We again find excellent agreement, with results consistent within the error bars (1σ). The modest differences arise from how the bolometric luminosity is partitioned: In the type-1 fits, more optical/UV emission is attributed to the AGN component, which changes the relative weight of the mid-IR constraints. However, as discussed before (Section 3.2), the optical/UV constraints are strongly degenerate with the stellar component. Because this choice does not produce a statistically significant change, we adopted the type-2 only fitting in the main analysis.

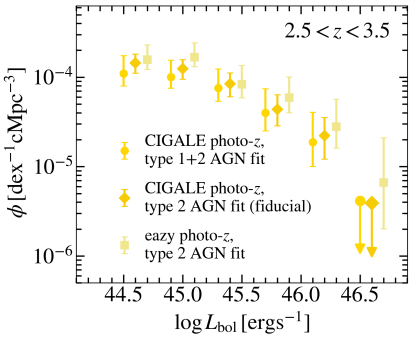


Figure B1. AGN luminosity function under different modeling assumptions. The points are shifted horizontally for better visualization. The yellow diamonds show our fiducial model, which uses `CIGALE` photometric redshifts for sources without spectroscopic redshifts and models the AGN emission with a type-2 template only. The yellow circles also use `CIGALE` photometric redshifts but additionally allow for a type-1 AGN component, while the yellow squares use `eazy` photometric redshifts and a type-2 AGN template only. Overall, we find good agreement among the three luminosity functions, with the largest discrepancies appearing at the highest luminosities, where the measurements are most affected by small number statistics.

Appendix C
Comparison with the AGN Identified in the JWST SMILES Program

Given the overlap of our analysis with the SMILES footprint, we cross-matched our AGN sample with the AGNs reported in J. Lyu et al. (2024). We note that there are some significant differences in the methodologies of the two studies, however. First, we require a detection in all F444W, F1000W, and F2100W in this work for the sources, meaning, e.g., that we do not include sources without F444W coverage, even if they show a clear MIRI detection. Second, the sample in J. Lyu et al. (2024) includes six additional MIRI filters (F560W, F770W, F1280W, F1500W, F1800W, and F2550W), providing additional depth compared to F1000W and F2100W alone. This allows them to probe lower luminosities and identify more sources that may be detected in other MIRI bands but not in F1000W and/or F2100W.

Additionally, the SED-fitting methodologies are different between the two studies. In J. Lyu et al. (2024), the SED fitting was performed with a modified Prospector framework that jointly models stellar emission, dust-obscured star formation, and AGN components, building on the Bayesian stellar-population inference framework of Prospector and FSPS (e.g., C. Conroy et al. 2009; J. Leja et al. 2019; B. D. Johnson et al. 2021). The fits were explored with dynamic nested sampling, and AGN classifications were retained only when the posterior solutions were well-behaved and consistent with the source photometry and morphology.

We show the results of the cross match in Figure C1. We recover 84 counterparts out of the 217 SMILES AGNs. As expected, the matched sources are those with bolometric luminosities above the F1000W and/or F2100W detection limits, while the majority of the unmatched objects fall below our sensitivity threshold. After visual inspection of all the cutouts, we identify six exceptions in which the lack of a match is not driven by sensitivity: Two sources fall outside the F444W coverage, and four are near a bright source and are not deblended by our source-detection procedure. We note, however, that our source injection simulations account for such incompleteness.

In the right panel of Figure C1, we compare the bolometric luminosities and redshift estimates derived by MEOW and SMILES. Our SED fitting generally yields lower bolometric luminosities, with a median of 0.5 dex difference compared to values reported by SMILES. Importantly, most of the sources driving these discrepancies lie outside the luminosity range that enters our luminosity-function and obscured-fraction analysis (Section 5), limiting their impact on the main results of this study. Given that both measurements rely on SED-fitting

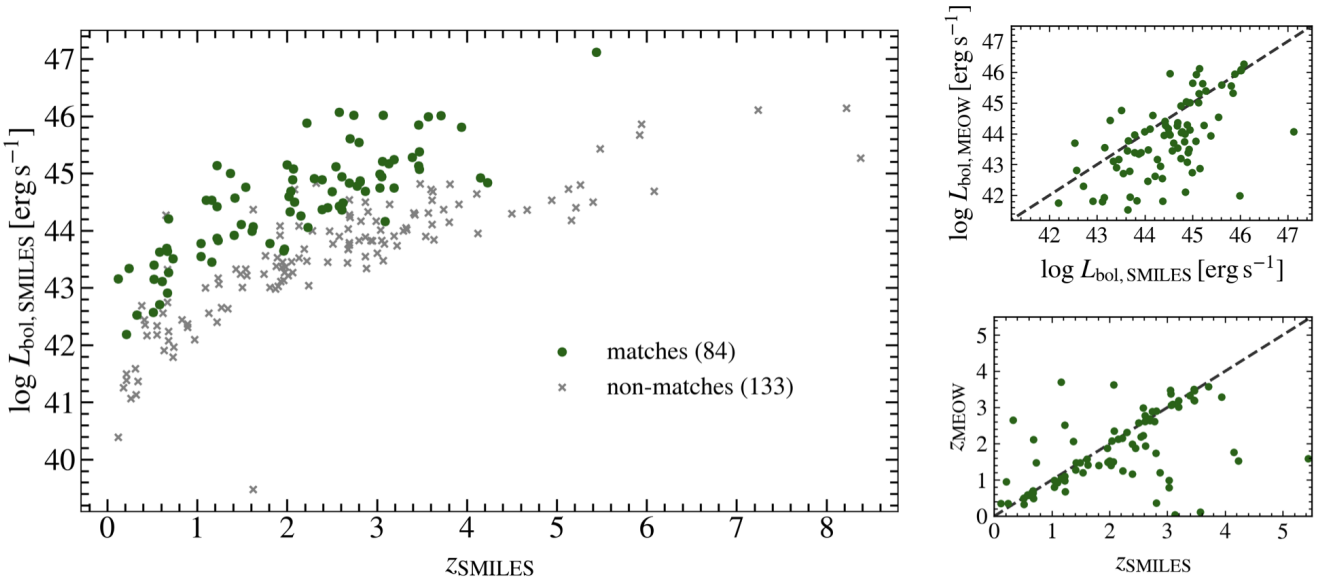


Figure C1. Comparison between the J. Lyu et al. (2024) AGN sample and this work, in the overlapping footprint. Out of the 217 AGNs identified in SMILES (J. Lyu et al. 2024), we find 84 counterparts in our sample. The unmatched AGNs are predominantly at the low-luminosity end, with six exceptions: Two lack F444W coverage and are therefore not identified in our sample, while four are affected by different deblending parameters in this work that result in only the brighter SMILES component being detected. Among the matched sources, we show the comparison between our luminosity and redshift estimates versus the SMILES counterparts, on the right.

methodologies, we do not attempt to determine which set of luminosities is more accurate; instead, we interpret the offsets as reflecting known systematic uncertainties in AGN SED modeling (e.g., J. Buchner et al. 2024). In this sense, our systematically lower bolometric luminosities would, if anything, render our inferred obscured fractions conservative. The redshift comparison shows substantially better overall agreement, with a small number of extreme outliers reaching $|\Delta z| \approx 4$. At the population level, these differences are not expected to materially affect our statistical conclusions (see also Appendix B).

Lastly, we note that 28 AGNs in our sample used for the luminosity-function analysis (Section 4) and lying within the SMILES footprint are not classified as AGNs in SMILES, which we attribute primarily to differences in the adopted SED modeling. We note that these 28 sources are uniformly spread in redshift but tend to be lower luminosities than the other MEOW AGNs in the same redshift bins. Furthermore, only 46 of the 84 cross-matched sources are independently identified as AGNs in our analysis (i.e., $f_{\rm AGN} > 0.1$). These systematic differences support the conclusion that our luminosity-function and obscured-fraction measurements are robust for reasonable variations in SED assumptions, but highlight the large uncertainties in inferring individual quantities via SED fitting.

ORCID iDs

Teodora-Elena Bulichi https://orcid.org/0000-0001-8174-6389
Gene C. K. Leung https://orcid.org/0000-0002-9393-6507
Anna-Christina Eilers https://orcid.org/0000-0003-2895-6218
Pablo G. Pérez-González https://orcid.org/0000-0003-4528-5639
Guillermo Barro https://orcid.org/0000-0001-6813-875X
Steven L. Finkelstein https://orcid.org/0000-0001-8519-1130
Micaela B. Bagley https://orcid.org/0000-0002-9921-9218
Anton M. Koekemoer https://orcid.org/0000-0002-6610-2048
Bren E. Backhaus https://orcid.org/0000-0001-8534-7502
Mark Dickinson https://orcid.org/0000-0001-5414-5131
Seiji Fujimoto https://orcid.org/0000-0001-7201-5066
Norman A. Grogin https://orcid.org/0000-0001-9440-8872
Dale D. Kocevski https://orcid.org/0000-0002-8360-3880
Ray A. Lucas https://orcid.org/0000-0003-1581-7825
Fabio Pacucci https://orcid.org/0000-0001-9879-7780
Nor Pirzkal https://orcid.org/0000-0003-3382-5941
Elia Pizzati https://orcid.org/0000-0002-9712-0038
Jan-Torge Schindler https://orcid.org/0000-0002-4544-8242
Alberto Traina https://orcid.org/0000-0003-1006-924X
Guang Yang (杨光) https://orcid.org/0000-0001-8835-7722

References

Alberts, S., Lyu, J., Shivaei, I., et al. 2024, ApJ, 976, 224
Alonso-Herrero, A., Pérez-González, P. G., Alexander, D. M., et al. 2006, ApJ, 640, 167
Andika, I. T., Jahnke, K., Onoue, M., et al. 2020, ApJ, 903, 34
Arita, J., Kashikawa, N., Matsuoka, Y., et al. 2023, ApJ, 954, 210
Assef, R. J., Stern, D., Kochanek, C. S., et al. 2013, ApJ, 772, 26
Astropy Collaboration, Price-Whelan, A. M., Lim, P. L., et al. 2022, ApJ, 935, 167
Astropy Collaboration, Price-Whelan, A. M., Sipőcz, B. M., et al. 2018, AJ, 156, 123
Astropy Collaboration, Robitaille, T. P., Tollerud, E. J., et al. 2013, A&A, 558, A33
Backhaus, B. E., Kirkpatrick, A., Yang, G., et al. 2025, AJ, 170, 300
Barlow-Hall, C. L., & Aird, J. 2025, arXiv:2506.16145
Begelman, M. C., & Volonteri, M. 2017, MNRAS, 464, 1102
Begelman, M. C., Volonteri, M., & Rees, M. J. 2006, MNRAS, 370, 289
Bennett, J. S., Sijacki, D., Costa, T., Laporte, N., & Witten, C. 2024, MNRAS, 527, 1033
Bertin, E., & Arnouts, S. 1996, A&AS, 117, 393
Boquien, M., Burgarella, D., Roehlly, Y., et al. 2019, A&A, 622, A103
Brammer, G. B., van Dokkum, P. G., & Coppi, P. 2008, ApJ, 686, 1503

Bromm, V., & Loeb, A. 2003, ApJ, 596, 34
Buchner, J., Georgakakis, A., Nandra, K., et al. 2015, ApJ, 802, 89
Buchner, J., Starck, H., Salvato, M., et al. 2024, A&A, 692, A161
Burlon, D., Ajello, M., Greiner, J., et al. 2011, ApJ, 728, 58
Bushouse, H., Eisenhamer, J., Dencheva, N., et al. 2022, JWST Calibration Pipeline, v1.8.5, Zenodo, doi:10.5281/zenodo.7429939
Calzetti, D., Armus, L., Bohlin, R. C., et al. 2000, ApJ, 533, 682
Casey, C. M. 2016, ApJ, 824, 36
Chabrier, G. 2003, ApJL, 586, L133
Conroy, C., Gunn, J. E., & White, M. 2009, ApJ, 699, 486
Daddi, E., Dannerbauer, H., Stern, D., et al. 2009, ApJ, 694, 1517
Davies, F. B., Hennawi, J. F., & Eilers, A.-C. 2019, ApJL, 884, L19
Davies, F. B., Hennawi, J. F., & Eilers, A.-C. 2020, MNRAS, 493, 1330
Donley, J. L., Koekemoer, A. M., Brusa, M., et al. 2012, ApJ, 748, 142
Draine, B. T., Aniano, G., Krause, O., et al. 2014, ApJ, 780, 172
Durodola, E., Pacucci, F., & Hickox, R. C. 2025, ApJ, 985, 169
Ďurovčíková, D., Eilers, A.-C., Chen, H., et al. 2024, ApJ, 969, 162
Ďurovčíková, D., Eilers, A.-C., Ishikawa, Y., et al. 2025, arXiv:2510.09753
Eilers, A.-C., Davies, F. B., & Hennawi, J. F. 2018, ApJ, 864, 53
Eilers, A.-C., Davies, F. B., Hennawi, J. F., et al. 2017, ApJ, 840, 24
Eilers, A.-C., Hennawi, J. F., Davies, F. B., & Simcoe, R. A. 2021, ApJ, 917, 38
Eilers, A.-C., Hennawi, J. F., Decarli, R., et al. 2020, ApJ, 900, 37
Eilers, A.-C., Mackenzie, R., Pizzati, E., et al. 2024, ApJ, 974, 275
Eisenstein, D. J., Willott, C., Alberts, S., et al. 2026, ApJS, 283, 6
Endsley, R., Stark, D. P., Lyu, J., et al. 2023, MNRAS, 520, 4609
Fan, X., Bañados, E., & Simcoe, R. A. 2023, ARA&A, 61, 373
Finkelstein, S. L., Bagley, M. B., Ferguson, H. C., et al. 2023, ApJL, 946, L13
Finkelstein, S. L., Leung, G. C. K., Bagley, M. B., et al. 2024, ApJL, 969, L2
Finkelstein, S. L., Ryan, R. E., Jr., Papovich, C., et al. 2015, ApJ, 810, 71
Fujimoto, S., Brammer, G. B., Watson, D., et al. 2022, Natur, 604, 261
Galametz, A., Grazian, A., Fontana, A., et al. 2013, ApJS, 206, 10
Giavalisco, M., Ferguson, H. C., Koekemoer, A. M., et al. 2004, ApJL, 600, L93
Gilli, R., Comastri, A., & Hasinger, G. 2007, A&A, 463, 79
Gilli, R., Norman, C., Calura, F., et al. 2022, A&A, 666, A17
Gordon, K. D., Sloan, G. C., Garcia Marin, M., et al. 2025, AJ, 169, 6
Grogin, N. A., Kocevski, D. D., Faber, S. M., et al. 2011, ApJS, 197, 35
Guo, X., Gu, Q., Fang, G., et al. 2026, A&A, 708, A157
Haiman, Z., Rees, M. J., & Loeb, A. 1997, ApJ, 476, 458
Hamblin, K., Kirkpatrick, A., Backhaus, B. E., et al. 2026, ApJ, 1002, 223
Harris, C. R., Millman, K. J., van der Walt, S. J., et al. 2020, Natur, 585, 357
Hickox, R. C., & Alexander, D. M. 2018, ARA&A, 56, 625
Hopkins, P. F., Hernquist, L., Cox, T. J., & Kereš, D. 2008, ApJS, 175, 356
Hopkins, P. F., Richards, G. T., & Hernquist, L. 2007, ApJ, 654, 731
Hsieh, C.-A., Goto, T., Ling, C.-T., et al. 2025, PASA, 42, e095
Huang, J., Hennawi, J., Pizzati, E., et al. 2026, arXiv:2602.04974
Hunter, J. D. 2007, CSE, 9, 90
Huško, F., Lacey, C. G., Roper, W. J., et al. 2025, MNRAS, 537, 2559
Inayoshi, K., Haiman, Z., & Ostriker, J. P. 2016, MNRAS, 459, 3738
Inayoshi, K., Visbal, E., & Haiman, Z. 2020, ARA&A, 58, 27
Iwasawa, K., Gilli, R., Vignali, C., et al. 2012, A&A, 546, A84
Iwasawa, K., Ricci, C., Privon, G. C., et al. 2020, A&A, 640, A95
Johnson, B. D., Leja, J., Conroy, C., & Speagle, J. S. 2021, ApJS, 254, 22
Juodžbalis, I., Maiolino, R., Baker, W. M., et al. 2026, MNRAS, 546, stag086
Kirkpatrick, A., Pope, A., Sajina, A., et al. 2015, ApJ, 814, 9
Kocevski, D. D., Finkelstein, S. L., Barro, G., et al. 2025, ApJ, 986, 126
Kodra, D., Andrews, B. H., Newman, J. A., et al. 2023, ApJ, 942, 36
Koekemoer, A. M., Faber, S. M., Ferguson, H. C., et al. 2011, ApJS, 197, 36
Kulkarni, G., Worseck, G., & Hennawi, J. F. 2019, MNRAS, 488, 1035
Lacy, M., Ridgway, S. E., Sajina, A., et al. 2015, ApJ, 802, 102
Lacy, M., Storrie-Lombardi, L. J., Sajina, A., et al. 2004, ApJS, 154, 166
Lawrence, A. 1991, MNRAS, 252, 586
Leitherer, C., Li, I.-H., Calzetti, D., & Heckman, T. M. 2002, ApJS, 140, 303
Leja, J., Johnson, B. D., Conroy, C., et al. 2019, ApJ, 877, 140
Leung, G. C. K., Bagley, M. B., Finkelstein, S. L., et al. 2023, ApJL, 954, L46
Leung, G. C. K., Eilers, A.-C., Endsley, R., et al. 2026, arXiv:2607.02666
Leung, G. C. K., Finkelstein, S. L., Pérez-González, P. G., et al. 2025, ApJ, 992, 26
Lin, X., Fan, X., Sun, F., et al. 2026, ApJ, 997, 61
Ling, C.-T., Goto, T., Kim, S. J., et al. 2026, PASP, 138, 014102
Liu, T., Tozzi, P., Wang, J.-X., et al. 2017, ApJS, 232, 8
Lupi, A., Haiman, Z., & Volonteri, M. 2021, MNRAS, 503, 5046
Lusso, E., Hennawi, J. F., Comastri, A., et al. 2013, ApJ, 777, 86
Lyu, J., Alberts, S., Rieke, G. H., et al. 2024, ApJ, 966, 229
Mazzolari, G., Gilli, R., Mignoli, M., et al. 2026, A&A, in press
Mazzucchelli, C., Bañados, E., Venemans, B. P., et al. 2017, ApJ, 849, 91
Merloni, A., Bongiorno, A., Brusa, M., et al. 2014, MNRAS, 437, 3550
Miller, T. B., Chapman, S. C., Aravena, M., et al. 2018, Natur, 556, 469
Morey, K. A., Eilers, A.-C., Davies, F. B., Hennawi, J. F., & Simcoe, R. A. 2021, ApJ, 921, 88
Mortlock, D. J., Warren, S. J., Venemans, B. P., et al. 2011, Natur, 474, 616
Ni, Q., Brandt, W. N., Yang, G., et al. 2021, MNRAS, 500, 4989
Ni, Y., Di Matteo, T., Gilli, R., et al. 2020, MNRAS, 495, 2135
Obuchi, S., Ichikawa, K., Yamada, S., et al. 2026, ApJ, 997, 156
Oesch, P. A., Brammer, G., Naidu, R. P., et al. 2023, MNRAS, 525, 2864
Östlin, G., Pérez-González, P. G., Melinder, J., et al. 2025, A&A, 696, A57
Pacucci, F., Ferrara, A., & Kocevski, D. D. 2026, arXiv:2601.14368
Pacucci, F., & Loeb, A. 2022, MNRAS, 509, 1885
Peca, A., Cappelluti, N., Urry, C. M., et al. 2023, ApJ, 943, 162
Peca, A., Koss, M. J., Oh, K., et al. 2025, ApJ, 990, 3
Pérez-González, P. G., Barro, G., Rieke, G. H., et al. 2024a, ApJ, 968, 4
Pérez-González, P. G., Rinaldi, P., Caputi, K. I., et al. 2024b, ApJL, 969, L10
Pezzulli, E., Valiante, R., & Schneider, R. 2016, MNRAS, 458, 3047
Pizzati, E., Hennawi, J. F., Schaye, J., et al. 2024, MNRAS, 534, 3155
Planck Collaboration, Ade, P. A. R., Aghanim, N., et al. 2016, A&A, 594, A13
Polletta, M., Weedman, D., Hönig, S., et al. 2008, ApJ, 675, 960
Pouliasis, E., Ruiz, A., Georgantopoulos, I., et al. 2024, A&A, 685, A97
Regan, J. A., Downes, T. P., Volonteri, M., et al. 2019, MNRAS, 486, 3892
Rieke, G. H., Alberts, S., Shivaei, I., et al. 2024, ApJ, 975, 83
Roberts, D., Shankar, F., Cammelli, V., et al. 2026, MNRAS, 546, stag223
Runnoe, J. C., Brotherton, M. S., & Shang, Z. 2012, MNRAS, 422, 478
Sajina, A., Lacy, M., & Pope, A. 2022, Univ, 8, 356
Sanders, D. B., Soifer, B. T., Elias, J. H., et al. 1988, ApJ, 325, 74
Satyavolu, S., Kulkarni, G., Keating, L. C., & Haehnelt, M. G. 2023, MNRAS, 521, 3108
Schindler, J.-T., Hennawi, J. F., Davies, F. B., et al. 2026, A&A, 708, A160
Shen, X., Hopkins, P. F., Faucher-Giguère, C.-A., et al. 2020, MNRAS, 495, 3252
Silverman, J. D., Mainieri, V., Ding, X., et al. 2023, ApJL, 951, L41
Simpson, C. 2005, MNRAS, 360, 565
Soltan, A. 1982, MNRAS, 200, 115
Stalevski, M., Fritz, J., Baes, M., Nakos, T., & Popović, L. Č. 2012, MNRAS, 420, 2756
Stalevski, M., Ricci, C., Ueda, Y., et al. 2016, MNRAS, 458, 2288
Stern, D., Eisenhardt, P., Gorjian, V., et al. 2005, ApJ, 631, 163
Szokoly, G. P., Bergeron, J., Hasinger, G., et al. 2004, ApJS, 155, 271
Taylor, A. J., Finkelstein, S. L., Kocevski, D. D., et al. 2025, ApJ, 986, 165
Trebitsch, M., Volonteri, M., & Dubois, Y. 2019, MNRAS, 487, 819
Trefoloni, B., Gilli, R., Lusso, E., et al. 2025, A&A, 697, A223
Treister, E., & Urry, C. M. 2006, ApJL, 652, L79
Ueda, Y., Akiyama, M., Hasinger, G., Miyaji, T., & Watson, M. G. 2014, ApJ, 786, 104
Vidal, E. P., Sajina, A., Banks, A. R., et al. 2026, ApJ, 1002, 23
Villa-Vélez, J. A., Buat, V., Theulé, P., Boquien, M., & Burgarella, D. 2021, A&A, 654, A153
Virtanen, P., Gommers, R., Oliphant, T. E., et al. 2020, NatMe, 17, 261
Vito, F., Brandt, W. N., Yang, G., et al. 2018, MNRAS, 473, 2378
Vito, F., Di Mascia, F., Gallerani, S., et al. 2022, MNRAS, 514, 1672
Vito, F., Gilli, R., Vignali, C., et al. 2014, MNRAS, 445, 3557
Volonteri, M. 2010, A&ARv, 18, 279
Volonteri, M., Lodato, G., & Natarajan, P. 2008, MNRAS, 383, 1079
Wang, F., Champagne, J. B., Huang, J., et al. 2026, ApJ, 1006, 39
Williams, C. C., Alberts, S., Ji, Z., et al. 2024, ApJ, 968, 34
Wise, J. H., Regan, J. A., O'Shea, B. W., et al. 2019, Natur, 566, 85
Wright, G. S., Rieke, G. H., Glasse, A., et al. 2023, PASP, 135, 048003
Yang, G., Boquien, M., Brandt, W. N., et al. 2022, ApJ, 927, 192
Yang, G., Boquien, M., Buat, V., et al. 2020, MNRAS, 491, 740
Yang, G., Caputi, K. I., Papovich, C., et al. 2023, ApJL, 950, L5
Yang, G., Papovich, C., Bagley, M. B., et al. 2021, ApJ, 908, 144
Zappacosta, L., Piconcelli, E., Duras, F., et al. 2018, A&A, 618, A28
Zou, F., Brandt, W. N., Chen, C.-T., et al. 2022, ApJS, 262, 15